

1

2       **Boundary-Layer-Coupled and Decoupled Clouds in Global Storm-**  
3       **Revolving Models: Comparisons with Field Observations**

4

5

6                   Tianning Su<sup>1</sup>, Yunyan Zhang<sup>1</sup>, Jingjing Tian<sup>2</sup>

7                   <sup>1</sup>Lawrence Livermore National Laboratory, Livermore, CA, USA

8                   <sup>2</sup>Pacific Northwest National Laboratory, Richland, WA, USA

9

10

11                  Submission to

12                  *Journal of Geophysical Research: Atmospheres*

13

14       \*Corresponding authors: [su10@llnl.gov](mailto:su10@llnl.gov)

15

16

17     **Abstract.** The accurate representation of interactions between the cloud and planetary  
18     boundary layer (PBL) is a persistent challenge in climate models, critical for simulating  
19     cloud evolution. The emergence of kilometer-scale Global Storm Resolving Models  
20     (GSRMs) promises enhanced details of PBL processes in these complex interactions.  
21     This study evaluates the representation of PBL-coupled and decoupled clouds in nine  
22     GSRMs simulations. Leveraging the Department of Energy Atmospheric Radiation  
23     Measurement program's extensive field observations across six sites with diverse  
24     meteorological backgrounds (SGP, SAIL, TRACER, ENA, GOAMAZON, and  
25     CACTI), we conducted an intercomparison of GSRMs with field observations. By  
26     differentiating coupling based on the relative positions between clouds and PBL, our  
27     analysis focuses on the simulation of cloud frequency, positions, and vertical extent.  
28     The GSRMs generally exhibit commendable agreement with observed cloud structures  
29     and PBL diurnal cycles across different sites. Compared to the relatively consistent  
30     representation of decoupled clouds, discrepancies are observed in the simulation of  
31     coupled clouds, particularly in areas of intense convection during the warm season such  
32     as GOAMAZON (the Amazon Forest) and CACTI (Sierras de Córdoba in Argentina).  
33     These biases are intimately associated with the models' tendency to underestimate  
34     boundary layer humidity and the convective initiation within different ranges of PBL  
35     heights. This study underscores the importance of improved representation of boundary  
36     layer convections within these high-resolution global models.  
37

38    **1    Introduction**

39        Clouds are fundamental to Earth's climate system, critically influencing radiative  
40        balance and climate feedback mechanisms (Betts, 2009; Teixeira and Hogan, 2002;  
41        IPCC, 2013, 2021; Fast et al., 2019). The interactions between clouds and the planetary  
42        boundary layer (PBL) are particularly significant, as low clouds frequently form within  
43        the PBL's entrainment zone under specific atmospheric conditions (Betts, 2009;  
44        Teixeira and Hogan, 2002; Golaz et al., 2002; Su et al., 2022a; Stull, 1988). Yet,  
45        accurately capturing these interactions in climate models, especially in the context of  
46        local-scale PBL processes, presents a notable challenge (Bretherton et al., 2007; Moeng  
47        et al., 1996; Su et al., 2023; Xian et al., 2023; Zheng et al., 2021; Zhang and Klein 2010,  
48        2013).

49        The development of Global Storm Resolving Models (GSRMs) has marked a  
50        significant step in climate modeling (Caldwell et al. 2021; Zängl et al. 2015; Klocke et  
51        al. 2017). These models, characterized by kilometer-scale resolutions such as the DOE's  
52        Simple Cloud-Resolving E3SM Atmosphere Model (SCREAM), offer an advanced  
53        approach to simulate convection processes, which were previously a significant  
54        challenge due to the coarse resolution of traditional models (Caldwell et al. 2021). By  
55        offering a more detailed representation of convection, GSRMs facilitate the explicit  
56        modeling of local-scale PBL evolution, crucial for the formation and evolution of  
57        convective systems (Houze, 2004; Lareau et al., 2018; Stevens et al. 2019; Betts, 2009;  
58        Golaz et al., 2002).

59        Despite the promise of GSRMs, several challenges persist. Traditional general

60 circulation models (GCMs) have long struggled with accurately simulating fine  
61 structures of cloud and precipitation processes due to their coarse resolution and  
62 reliance on parameterized convection (Eyring et al., 2016; Moncrieff, 2010; Fan et al.,  
63 2017). GSRMs, with their finer resolution, aim to address these issues by reducing  
64 longstanding biases in cloud and precipitation modeling, as evidenced in the  
65 DYAMOND (DYnamics of the Atmospheric general circulation Modeled On Non-  
66 hydrostatic Domains) project (Stevens et al., 2019, 2020; Roh et al., 2021; Judt et al.,  
67 2021). However, the representation of smaller-scale processes, such as PBL turbulence,  
68 cloud microphysics, and aerosol interactions, remains an area for further improvement  
69 (Bretherton et al., 2007; Moeng et al., 1996).

70 This fine resolution of GSRMs offers a unique opportunity for model evaluation  
71 through direct comparison with point-based observations, a task that was challenging  
72 with coarser GCMs. For this purpose, the Department of Energy's Atmospheric  
73 Radiation Measurement (ARM) program provides unique resources for such  
74 evaluations. ARM program offers extensive observations across multiple observatories  
75 and mobile facilities and captures a wide range of meteorological conditions. Thus, it  
76 provides an ideal platform for exploring the interactions between the PBL and clouds,  
77 facilitating direct comparisons with GSRMs.

78 This study, positioned within the Tying in High Resolution E3SM with ARM Data  
79 (THREAD) project, uses these high-resolution simulations from GSRMs to scrutinize  
80 the representation of coupled and decoupled boundary layer clouds within the ambit of  
81 the DYAMOND initiative. This analysis of PBL convections and boundary layer clouds

82 aims to systematically examine cloud-land interactions across varied cloud regimes and  
83 states of coupling. These endeavors seek to highlight the capacities and constraints of  
84 GSRMs in simulating the complexities of PBL convections and clouds, and thus,  
85 contribute to the potential refinement of climate modeling practices with an emphasis  
86 on the coupling between clouds and PBL.

87

## 88 **2 Data and Method**

### 89 *2.1 DYAMOND Global Storm-Resolving Models*

90 This study leverages the vast data repository of DYAMOND initiative. We utilize  
91 high-resolution simulations from multiple models to investigate the detailed  
92 interactions between PBL and cloud formations within the GSRMs. Within the  
93 framework of DYAMOND, GSRMs operate at kilometer-scale resolution, ranging from  
94 2.5 to 5.0 km, a significant enhancement over traditional GCMs. This leap in resolution  
95 allows for the explicit representation of convective processes and complex cloud  
96 systems without relying heavily on parameterization schemes. The initiative's Phase-II  
97 winter uses the European Center for Medium-Range Weather Forecasts (ECMWF)  
98 Integrated Forecasting System for initialization.

99 We used nine GSRM simulations for the analysis, including UM, SCREAM, gSAM,  
100 IFS, ICON, SHIELD, GEOS, GEM, and ARPEGE. Their horizontal grids and affiliated  
101 institutions are listed in Table 1. Detailed information about the DYAMOND initiative  
102 and the participating models can be found in Stevens et al. (2019), while the individual  
103 model configurations can be found in the references listed in Table 1.

104      Initiated on January 20, 2020, these simulations spanned 40 days. This study starts  
105      to use model simulations since the third day to allow an initial spin up period. These  
106      simulations were carefully configured to span a range of horizontal and vertical  
107      resolutions and included various physics parameterization schemes, designed to capture  
108      the characteristics of atmospheric convections. The models' horizontal resolutions,  
109      which ranged from 3.0 to 5.0 km, provide a detailed examination for PBL and cloud at  
110      a fine scale.

111      In our methodology for identifying cloud base height and determining cloud  
112      fraction, we used vertical profiles of mass fraction of cloud ice and mass fraction of  
113      cloud liquid water. Aligning with the threshold used in the ECWMF's fifth-generation  
114      global reanalysis (ERA-5, Hersbach et al., 2020), cloud base height is identified where  
115      cloud liquid water content or cloud ice water content exceeds  $10^{-6}$  kg/kg, while  
116      excluding fog by disregarding cloud presence at the model's lowest level. In the same,  
117      the cloudy condition is defined as cloud liquid water content or cloud ice water content  
118      exceeds  $10^{-6}$  kg/kg. Due to the inconsistent definition and absence of direct cloud  
119      fraction outputs in some models, we adopted a binary diagnostic approach. This means  
120      cloud fractions are treated as 1, if cloud liquid water or cloud ice water content is greater  
121      than  $10^{-5}$  kg/kg, otherwise cloud fraction is treated as 0. It offers a simplified yet  
122      effective method for comparing cloud fractions across various model simulations.

123

124     *2.2 ARM observations*

125       This study extensively utilizes observations from six ARM field campaigns,  
126       including SGP, SAIL, TRACER, ENA, GOAMAZON, and CACTI. It provides diverse  
127       conditions in climatic and geographical settings. The locations of these sites are marked  
128       in Figure 1.

129       (1)      Southern Great Plains (SGP): Located in the central United States, the SGP  
130       site is ARM's oldest and most extensive observatory, providing information of  
131       continental cloud formations for more than two decades.

132       (2)      The Surface Atmosphere Integrated Field Laboratory (SAIL) set in Colorado's  
133       East River Watershed, focuses on dissecting atmospheric and hydrological processes  
134       within mountainous regions from September 2021 to June 2023.

135       (3)      Tracking Aerosol Convection Interactions Experiment (TRACER): Conducted  
136       in the Houston October, 2021, to September, 2022, Texas area, TRACER emphasizes  
137       the interactions between urban aerosols, convection, and clouds.

138       (4)      Eastern North Atlantic (ENA): The ENA site, situated on Graciosa Island in  
139       the Azores, offer long-term datasets for studying marine cloud systems and their  
140       influence on the North Atlantic climate since 2013.

141       (5)      Green Ocean Amazon (GOAMAZON): This campaign investigates the  
142       tropical cloud lifecycle and atmospheric composition over the Amazon rainforest  
143       from Jan, 2014 to Nov, 2015.

144 (6) Cloud, Aerosol, and Complex Terrain Interactions (CACTI): Located in the  
145 Sierras de Córdoba mountain range in Argentina, CACTI capture the cloud systems that  
146 form over complex terrain from Oct, 2018 to Apr, 2019.

147 For our analysis, we sourced observational data from various ARM campaign  
148 datasets, encompassing measurements such as cloud base and top heights, cloud  
149 fraction, and surface sensible and latent heat fluxes, alongside PBL height metrics.  
150 Radiosonde data were instrumental in detailing the PBL's thermodynamic profiles, with  
151 routine launches at ARM sites offering vital insights into atmospheric conditions. The  
152 technical aspects of ARM's radiosonde measurements are documented by Holdridge et  
153 al. (2011). It's important to note that radiosonde launch frequencies vary across different  
154 sites. Specifically, for the SGP, TRACER, and GOAMAZON sites, radiosondes are  
155 routinely launched at 0, 12, and 18 UTC. At the SAIL and ENA, launches occur at 0  
156 and 12 UTC. For the CACTI site, radiosondes are launched more frequently, at 0, 12,  
157 15, 18, and 21 UTC during the field campaign. We analyzed radiosonde data from  
158 within one hour of these specified times for analysis at each site. For direct comparisons  
159 with GSRMs, we align our analysis to correspond with these same observational times,  
160 ensuring consistency in the model evaluation.

161 Furthermore, the ARM program's ARSCL (Active Remote Sensing of Clouds)  
162 product amalgamates data from Micropulse Lidar (MPL), ceilometers, and cloud radars,  
163 presenting an integrated view of cloud vertical structure and their temporal dynamics  
164 as detailed by Clothiaux et al. (2000) and further analyzed by Kollias et al. (2007). For  
165 the most accurate cloud base measurements, we prioritized laser-based detections from

166 MPL and ceilometers. The cloudy pixels are defined as cloud fraction above 1%.  
167 Drawing on the ARSCL data, Xie et al. (2010) compiled an extensive record of cloud  
168 fraction profiles, which, along with surface meteorological observations and flux  
169 measurements from ARM BEST ESTIMATE DATA PRODUCTS (ARMBE),  
170 provided a comprehensive dataset for our study.

171 To assess the capabilities of GSRMs in simulating PBL and cloud, we select GSRM  
172 outputs that fall within a 10-km radius of ARM observation sites. To ensure a coherent  
173 comparison, we utilized data from ARM observations during the same calendar period  
174 (20 January to 28 February) across different years to build the climatology, juxtaposed  
175 against the corresponding model output period.

176

### 177 *2.3 Determination of PBL height and Cloud Coupling*

178 In our study, we identify the PBLH and the cloud coupling with the PBL using the  
179 same approach in both model and observations. To calculate PBLH, we adopted the  
180 bulk Richardson number ( $Ri$ ) method, following the approach used by Seidel et al.  
181 (2012) and Vogelegang and Holtslag (1996). The  $Ri$  method, suitable for both stable  
182 and convective boundary layers, facilitates the estimation of PBLH across extensive  
183 datasets from radiosonde and model data, proving to be highly effective for PBLH  
184 climatology analysis due to its applicability to varied atmospheric conditions. The  
185 Richardson number ( $Ri$ ) is defined as follows:

$$186 \quad Ri(z) = \frac{(g/\theta_{vs})(\theta_{vz} - \theta_{vs})(z - z_s)}{(u_z - u_s)^2 + (v_z - v_s)^2 + (bu_*^2)}$$

187 where  $z$  represents the height above ground level,  $s$  denotes the surface,  $g$  is the  
188 acceleration due to gravity,  $\theta_v$  indicates virtual potential temperature, and  $u$  and  $v$  are  
189 eastward and northward wind components. Meanwhile,  $u^*$  indicates surface friction  
190 velocity and is considered negligible because its magnitude is significantly smaller  
191 compared to the bulk wind shear term in the denominator (Vogelezang and Holtslag.  
192 1996). The Richardson number ( $Ri$ ) is dimensionless and serves not to quantify the  
193 intensity of turbulence but to signal its presence or absence. According to theoretical  
194 and empirical studies, such as those by Stull (1988), turbulence is initiated when  $Ri$   
195 falls below a critical threshold (0.25), indicating the transition from laminar to unstable  
196 flow. Consequently, in this study, PBLH is determined at the lowest  $z$  where the  
197 interpolated  $Ri$  crosses the critical value of 0.25, aligning with the approach adopted by  
198 Seidel et al. (2012).

199 Figure 1 provides an example of the PBL height (PBLH) across the globe from the  
200 ECMWF IFS at kilometer-scale resolution. Here, PBLH is directly obtained from the  
201 model output, which also use Richardson number method with a threshold 0.25  
202 (Roberts et al., 2018). It reveals the detailed spatial distribution of PBLH, highlighting  
203 the model's proficiency in capturing the PBL characteristics in a fine resolution. The  
204 ability to represent these spatial variations is important, given that the PBL is driven by  
205 local-scale processes often inadequately represented at coarser resolutions. Our  
206 evaluation aims to determine the extent to which GSRM-simulated PBL processes,  
207 including PBL height, correspond with observations across diverse metrics.

208 In our methodology, the distinction between coupled and decoupled clouds is  
209 fundamental to understanding the interactions between the cloud base and the PBL (Su  
210 et al. 2022b). Clouds are defined as coupled when the turbulence originating from the  
211 surface are able to reach the cloud base, hence affecting its evolution, resulting in a  
212 turbulence-facilitated linkage among surface fluxes, PBL, and the cloud. This is  
213 contrasted with decoupled clouds, which are characterized by a temperature inversion  
214 between the PBL top and the cloud base. These clouds form in conditions that are  
215 largely independent of surface-driven processes, as evidenced by the weak relationship  
216 between cloud, PBL, and surface forcing (Su et al. 2023, 2024).

217 To systematically categorize clouds as coupled or decoupled, we employ a  
218 straightforward criterion based on the vertical distance between the cloud base height  
219 (CBH) and PBLH. A cloud is considered decoupled if the difference between CBH and  
220 PBLH exceeds 0.2 km. Conversely, a cloud is deemed coupled if this vertical distance  
221 is less than 0.2 km. This classification, as evaluated by Su et al. (2022b), provides an  
222 efficient and effective means to distinguish between the two regimes, offering clarity  
223 on the nature of cloud-PBL interactions within the context of land-atmosphere coupling.  
224 This methodological framework allows for an investigation into the cloud-PBL  
225 coupling for both models and observations.

226

227    **3    Results**

228    *3.1 Diurnal Cycles of PBLH and Cloud Fractions in Observations and Models*

229    To provide a foundation for understanding PBL-coupled clouds, our study first  
230    examines the climatology of PBL heights and cloud fractions between observations and  
231    models. Figure 2 presents the statistical mean of PBLH from radiosonde over six sites,  
232    juxtaposing the diurnal cycles of GSRMs. The ensemble mean of GSRMs demonstrates  
233    a good agreement with observed PBLH. This agreement demonstrates the proficiency  
234    of GSRMs in replicating essential diurnal cycles of PBLH. While the ensemble mean  
235    of GSRMs generally aligns well with observations, individual model outputs exhibit  
236    significant variations, underscoring the diversity in model behavior. Notably, the ICON  
237    model predicts a lower PBL height, especially at the SGP site, where its daily maximum  
238    hovers around 0.5 km, in contrast to other models which suggest a PBL height closer to  
239    1 km. Meanwhile, SCREAM demonstrates a tendency to overestimate PBLH for the  
240    SGP and CACTI sites, highlighting distinct biases among individual model  
241    performances.

242    It's important to note that the climatology presented here may include sampling  
243    biases due to the differing periods over which field observations and model simulations  
244    were conducted. While the observational data spans different periods (See Section 2.2),  
245    the model outputs are specifically from the year 2020. However, such sampling biases  
246    will not significantly alter the mean diurnal cycle of the PBL. This assumption is  
247    supported by separate analyses of observational and model samples within the ERA-5

248 dataset, which show no notable differences in the calculated PBLH diurnal cycles  
249 (Figure S1).

250 We further dive into the diurnal cycles of cloud fraction profiles for observational  
251 data and the ensemble outputs of GSRMs (Figure 3 and Figure 4). This comparison  
252 demonstrates some disparities in cloud fraction between observation and models for  
253 different regions. Specifically, at the SGP site, the observations present a large amount  
254 of high clouds. GSRMs produce lower fractions for the middle-level and high-level  
255 clouds, despite a good consistency in low-level clouds. Conversely, at SAIL and  
256 TRACER, there's a consistent underestimation by GSRMs of low-cloud coverage. For  
257 SAIL, clouds in GSRMs also demonstrate a relatively lower position compared to the  
258 observations.

259 Figure 4 extends similar analyses for the ENA, GOAMAZON, and CACTI sites.  
260 GSRMs face notable challenges in simulating low-level clouds, especially for  
261 GOAMAZON and CACTI, where the models significantly underrepresent the  
262 boundary layer clouds. GOAMAZON is a region with frequent deep convection in this  
263 region (Tian et al. 2022). For this region, we noted the consistent underestimation of  
264 cloud fraction from low to high levels. this discrepancy might be rooted in the models'  
265 inability to simulate the transitions from shallow to deep convection accurately, a  
266 critical process for cloud formation and evolution.

267 These analyses reveal that while GSRMs show promise in simulating diurnal PBL  
268 and cloud fraction cycles, notable discrepancies in cloud fraction between observations  
269 and models in different regions underscore the need for improving cloud simulations in

270 models. This comparison also highlights a potential limitation in representing cloud-  
271 PBL interaction models as noted by the significant underestimation of boundary layer  
272 clouds for CACTI and GOAMAZON. This issue has been further illuminated in the  
273 following sections.

274

275 *3.2 Coupled and Decoupled Clouds in GSRMs*

276 This section demonstrates the general characteristics of coupled and decoupled  
277 clouds. As the determination of PBL-coupled clouds is based on the relative position  
278 between clouds and PBL, Figure 5 delves into the frequency of the CBH-PBLH under  
279 different ranges, which can be a key indicator for the coupled and decoupled cloud  
280 states. In addition to the comparison of the ensemble mean of GSRMs, the cloud  
281 frequency around PBLH for individual nine models for different sites are detailed in  
282 Figure S2-S7. Comparing observations from six sites against the GSRMs demonstrates  
283 a general pattern in the simulating coupled clouds between the model and observations.  
284 Clouds frequently form around the top of PBL, as indicated by the peak spectrum of  
285 CBH frequency around the PBLH.

286 The large amount of clouds around the PBL top indicates the coupling between  
287 clouds and clouds. As indicated in Section 2.3, a 200-meter threshold for CBH-PBLH  
288 is used to distinguish the coupled and decoupled regimes (grey dash lines in Figure 5).  
289 The ensemble mean of GSRMs demonstrates a consistent pattern with observations  
290 over the SGP and TRACER. For SAIL, despite a relatively similar peak in cloud  
291 frequency for the coupled regime, the cloud positions demonstrate some differences

292 between observations and models. Similar to the results of Figure 2d-f, the model  
293 produces a lower position of clouds, and high cloud fraction near the surface for SAIL.  
294 However, this situation notably differs at the CACTI, GOAMAZON, and ENA sites,  
295 where a noticeable gap emerges between the model and observations, as models notably  
296 underestimate the cloud frequency around the PBL, indicating the insufficient coupled  
297 clouds in GSRMS. These disparities are possibly caused by models' ability to accurately  
298 simulate cloud microphysics and turbulent processes. This comparison noted both the  
299 agreement and disparities between observations and GSRMs, highlighting the  
300 importance of improved representation of cloud-PBL interactions in models for  
301 convective active regions, such as GOAMAZON and CACTI.

302 We further examine the vertical profiles of thermodynamics for coupled and  
303 decoupled clouds in GSRMs and field observations in Figure 6. We normalized the  
304 profiles based on the CBH and presented the averaged profiles for the sub-cloud layer.  
305 To ensure sufficient samples. We only analyzed the cloud base above 0.2 km.  
306 Meanwhile, since cloud position shows a large difference between the model and  
307 observations for SAIL possibly due to the complexity of resolving mountain topography,  
308 we average the results from the other five sites.

309 In Figure 6a, the vertical profiles of potential temperature for coupled clouds show  
310 relatively uniform values beneath the cloud base, reflecting an unstable layer marked  
311 by turbulent heat and moisture conditions. This instability is also demonstrated by the  
312 relatively uniform distribution of moisture observed in Figure 6c and Figure 6e for  
313 coupled clouds, which is indicative of a layer undergoing active convective mixing

314 below the cloud base. There are significant upward fluxes of heat and moisture typical  
315 for coupled cloud formations. In contrast, decoupled clouds are distinguished by a  
316 notable temperature inversion above the cloud base, which acts to suppress vertical  
317 mixing and the transfer of heat and moisture in the sub-cloud layer, as evidenced by the  
318 diminishing moisture content with increasing altitude.

319 Despite the general consistency between observations and models, the potential  
320 temperature for coupled clouds is warmer for the coupled clouds, possibly associated  
321 with the warm biases reported in the previous studies (Qin et al. 2023; Lin et al., 2017;  
322 Ma et al., 2018). Meanwhile, relative humidity (RH) is slightly lower in terms of peak  
323 value at the cloud base for the observations, which can be attributed to the drift of the  
324 sonde balloon. To sum up, these thermodynamic profiles of coupled and decoupled  
325 clouds support a clear dichotomy in classifying cloud coupling states and underscore  
326 the importance of representing cloud coupling in GSRMs.

327

### 328 *3.3 Difference in Cloud Frequency and Fractions among Different Models*

329 We further examine the coupled and decoupled clouds for different models. Figure  
330 7 presents the variance in coupled cloud frequencies from various GSRMs compared to  
331 different field campaign observations. This analysis demonstrates the GSRMs'  
332 tendency to underestimate the frequency of coupled clouds at ENA, TRACER, and  
333 GOAMAZON sites. Different models show disparate performance for different regions.  
334 We noted some notable differences here. In particular, several models, including ICON,  
335 UM, and ARPEGE, show a substantial overestimation of coupled clouds for SGP and

336 SAIL but significantly underestimate the coupled clouds for ENA, GOAMAZON, and  
337 CACTI. SHiELD and gSAM demonstrate relatively low cloud frequency for all sites.

338 The standard deviation of interannual variabilities for SGP and ENA are noted in  
339 Figure 7. In general, the interannual variabilities or sampling biases between  
340 observations and GSRMs should not significantly affect the results. As noted in Figure  
341 S8. the sample biases between observations and GSRMs would lead to less than 10%  
342 in coupled cloud frequency, except for SAIL with 30% difference between the model  
343 and observation periods. It further confirmed the notable underestimations of coupled  
344 clouds for GOAMAZON and CACTI in GSRMs, which are confirmed by both  
345 observations and ERA-5 datasets. It highlights the need for addressing the  
346 underrepresentation of coupled cloud frequencies in GSRMs.

347 We further explore the vertical distribution of coupled cloud fractions in GSRMs  
348 and field observations in Figure 8. Here, the coupled cloud is defined as those clouds  
349 rooted in PBL, which means if the cloud base is below 0.2 km plus PBL top regardless  
350 of the cloud's vertical extent. This examination is important for evaluating GSRMs'  
351 capacity to simulate the structures of coupled clouds. At the SGP site, models generally  
352 align well with observations, capturing the extensive coupled clouds in the lower  
353 tropospheric, despite significant overestimations in coupled clouds for UM and ICON.  
354 However, discrepancies emerge, such as at the SAIL site, where models consistently  
355 simulate coupled clouds at lower altitudes than observed, revealing a gap in accurately  
356 capturing cloud height.

357 Further challenges are evident at the TRACER, ENA, GOMAZON, and CACTI

358 locations, where GSRMs tend to underestimate coupled cloud fractions. For TRACER  
359 and ENA, such disparities are demonstrated for the coastal and marine environment  
360 with a relatively small diurnal cycle of PBL, associated with the regimes of  
361 stratocumulus. GSRMs, both underestimate the vertical spread and peak fraction for  
362 these two sites. It also demonstrates difficulties in accurately simulating cloud fraction  
363 for this coupled cloud for a convective environment, as the results of GOAMAZON  
364 and CACTI represent the climatology in the warm season. The situation for  
365 GOAMAZON is also associated with deep convection. Deep convection is active for  
366 this region and is usually coupled with PBL. Thus demonstrates a consistently high  
367 coupled cloud fraction from low to middle-level clouds. However, GSRMs do not  
368 demonstrate this feature with a much lower fraction of coupled clouds at different levels.

369 We also present the vertical distribution of decoupled cloud fractions by comparing  
370 the simulation from GSRMs against the climatology of field observations in Figure 9.  
371 Decoupled clouds exhibit more weak links to the PBL and surface forcing, often either  
372 emerging as residuals from land-coupled convective systems or being influenced  
373 predominantly by horizontal advectons. These clouds also greatly contribute to the  
374 convective system and radiation budgets. Our analyses indicate that GSRMs produce a  
375 similar structure compared with the observed climatology of decoupled clouds for  
376 different sites. Meanwhile, differences still exist, especially for the SGP, observation  
377 indicates a much larger amount of decoupled high clouds compared to the models  
378 (Figure 9a). However, these underestimation of ice clouds are not likely related to the  
379 PBL and local-scale forcing.

380        Significant discrepancies are observed at two regions with active convection:  
381        GOAMAZON and CACTI. There is a notable overestimation of decoupled low clouds  
382        in GSRMS (Figure 9e-f). In these regions, observations suggest a dominance of PBL-  
383        coupled clouds in the low cloud regime, whereas GSRMs tend to classify a substantial  
384        portion of these clouds as decoupled. This misclassification underscores potential  
385        shortcomings within the models in capturing the coupling states of low clouds for active  
386        cumulus or deep convection environments. These findings accentuate the importance  
387        of refining GSRMs' simulations of coupling states to bridge the gap between model  
388        outputs and observational data for cloud vertical distribution.

389

### 390        *3.4 Linkage between Clouds, Humidity, and PBL*

391        To delve deeper into the mechanisms behind model-observation discrepancies in  
392        cloud representation, this section explores the linkage between clouds, humidity, and  
393        PBL as depicted in GSRMs and observed data. The ensemble mean of GSRMs shows  
394        the consistent PBLH climatology with observations. We attempt to examine the  
395        systematic biases of humidity and surface in GSRMs.

396        Figure 10 presents the diurnal cycles of surface RH ( $RH_{surf}$ ) and PBL mean RH  
397        ( $RH_{bl}$ ) from GSRMs and observations across different sites. This exploration reveals  
398        the agreement in RH between GSRMs and observations at TRACER and ENA.  
399        However, for other sites, notable discrepancies in GSRMs are noted, particularly at  
400        CACTI and GOAMAZON, where models consistently underrepresent RH levels within  
401        the PBL. This underestimation highlights potential gaps in the models' ability to

402 simulate the complex moisture variations and feedback mechanisms characteristic of  
403 these regions, potentially impacting the accuracy of cloud formation and evolution  
404 predictions. Conversely, at sites like SGP and SAIL, an overestimation of RH suggests  
405 models may overly emphasize moisture accumulation processes.

406 These biases of GSRMs are contributed by individual models. As detailed in Figure  
407 S9, ICON, and UM exhibit an overestimation of RH for the SGP and SAIL,  
408 corresponding to notable overestimations of coupled clouds in these models for these  
409 regions. On the other side of the spectrum, models including IFS, GEM, and UM tend  
410 to contribute to an overall underestimation of RH for GOAMAZON, affecting the  
411 ensemble mean and indicating a potential systematic dry bias in these models.  
412 SCREAM notably underestimates RH for both SGP and CACTI, aligning with its  
413 relatively low coupled cloud frequencies there. As noted in Figure S10, the differences  
414 in samples between models and observations can lead to a relatively small difference  
415 (0-10%) in ERA-5, indicating the observation-model differences are not dominated by  
416 the sampling biases.

417 Figure 11 demonstrates the diurnal surface variations of sensible and latent heat flux  
418 variations in GSRMs and field observations. These surface fluxes are important for  
419 model simulations, as they dictate the crucial energy exchanges between the earth's  
420 surface and atmosphere. Although the same period (20 Jan to 28 Feb) is utilized for  
421 observational data across this study, for GOAMAZON, observations of surface fluxes  
422 for the entire months of January and February are averaged due to insufficient sampling.  
423 For reference, the surface fluxes in different models are presented in Figure S11 and

424 Figure S12. The analysis reveals a pattern of overestimation in latent heat fluxes by  
425 GSRMs at sites like CACTI, GOAMAZON, and SAIL. This suggests surface fluxes  
426 are not likely the major factors contributing to the underestimation of coupled clouds,  
427 as the strong latent heat in the model should facilitate the growth and development of  
428 convective clouds (Zhang and Klein, 2013).

429 For two mountain sites (i.e., SAIL and CACTI), observed surface fluxes are  
430 generally smaller than the GSRMs, highlighting potential challenges in how models  
431 resolve mountain surface processes at high resolution. However, it is also important to  
432 note that the complexity of comparing localized observational data with the grids of  
433 model outputs poses significant challenges, emphasizing the need for careful  
434 consideration of scale and representativeness in site measurements. For example, Tang  
435 et al. (2019) noted the large differences in surface fluxes between two sites with a  
436 difference of around 100m. Hence, we cannot conclude the differences between the  
437 model and observations in terms of surface fluxes represent the model biases. These  
438 analyses are used to support that the surface fluxes are not likely the major problem in  
439 the underestimation of coupled clouds for GOAMAZON and CACTI.

440 Cloud development across various coupling regimes is linked to essential  
441 meteorological factors, particularly atmospheric instability and humidity, as indicated  
442 by PBLH and surface RH. Figure 12 indicates the corresponding variations in the  
443 frequency of low clouds under different values of PBLH and RH in GSRMs and  
444 observations. In this analysis, low clouds only indicate the cloud base is less than 4.5km

445 and do not consider the vertical extent. This examination aims to reveal the impacts of  
446 humidity and PBL on the low cloud formations. From both GSRMs and observations,  
447 the analysis demonstrates the close linkage between RH, PBLH, and the formation of  
448 coupled clouds. The trigger of coupled clouds is dictated by turbulence and humidity,  
449 and both high RH and PBLH contribute to the formation of coupled clouds. Specifically,  
450 stratiform clouds are likely to form in the high RH<sub>surf</sub> conditions, while the cumulus  
451 forms in the high PBLH scenarios with well-developed unstable sub-cloud layers (Su  
452 et al. 2024). Such findings emphasize the moisture exchange and thermal convection as  
453 critical drivers for coupled cloud formation.

454 Unlike coupled clouds, which demonstrate a clear linkage between cloud formation  
455 frequency and both surface and PBL humidity (RH<sub>surf</sub> and RH<sub>bl</sub>), the decoupled low  
456 cloud frequency does not show notable relationships with these humidity variables  
457 (Figure 12 and Figure S13). This lack of association suggests that the humidity within  
458 the PBL does not play a supportive role in the development of decoupled low clouds.  
459 Instead, these clouds tend to exhibit a higher frequency under the low PBLH, implying  
460 that weak local convection or high atmospheric stability, conditions contrary to those  
461 favorable for coupled cloud formation, are conducive to the occurrence of decoupled  
462 low clouds. This distinct behavior underscores the different mechanisms driving the  
463 formation of decoupled versus coupled clouds

464 Moreover, Figure 12 demonstrates certain discrepancies between model outputs and  
465 observations, most notably in the tendency of GSRMs to underestimate RH<sub>surf</sub> for

466 GOAMAZON and CACTI. Such underestimation can lead to the underestimation of  
467 coupled clouds. Meanwhile, under the similar ranges of PBLH and RH, GSRMs also  
468 tend to trigger insufficient coupled clouds. Such biases are directly related to the model  
469 parameterization suggesting the need to enhance representation of coupled cloud  
470 occurrence. Compared to the coupled clouds, GRSMs produce a similar frequency in  
471 terms of decoupled low clouds with observations. It also should be noted that using  
472 RH<sub>surf</sub> or RH<sub>bl</sub> will not change the findings in this analysis (Figure S13).

473 Following the insufficient trigger of coupled clouds, Figure 13 delves into the  
474 details of how coupled clouds form within various GSRMs. This comparative analysis  
475 via contour plots elucidates the specific environmental thresholds that each model  
476 associates with a 50% probability of coupled cloud occurrence, shedding light on the  
477 impacts of cloud-PBL interactions on the coupled cloud trigger. By comparing the 50%  
478 occurrence rate of coupled clouds between models and observations, we can  
479 demonstrate whether models have sufficient coupled clouds under the same range of  
480 PBLH and RH<sub>surf</sub> compared with observations.

481 Several models, specifically UM, SCREAM, IFS, and ARPEGE, exhibit coupled  
482 cloud frequencies that align closely with those observed, indicating their effective  
483 replication of coupled cloud formation under comparable ranges of PBLH and RH to  
484 observations. In contrast, models like gSAM, ICON, and SHiELD show a marked  
485 deficiency in simulating sufficient coupled clouds, especially underestimating coupled  
486 cloud frequency under a high PBLH scenario (Figure 13c, e, f). This discrepancy is

487 highlighted by the requirement for significantly higher RH and PBLH levels in these  
488 models to achieve a 50% frequency of coupled clouds, unlike the observations. A  
489 similar conclusion is drawn when analyzing RH within the PBL ( $RH_{bl}$ ), as shown in  
490 Figure S14.

491

#### 492 **4. Conclusions**

493 This study carries out a detailed examination of PBL-coupled and decoupled clouds  
494 in nine GSRMs and compares them with the rich observational datasets from fixed sites  
495 or field campaigns within DOE's ARM program, including SGP, SAIL, TRACER, ENA,  
496 GOAMAZON, and CACTI. Our investigation spanned from the diurnal cycles of  
497 PBLH and cloud fractions to the representation of cloud-PBL relationships in models,  
498 unveiling both the strengths and limitations of current GSRM simulations.

499 Key findings from our work reveal that, while GSRMs well capture the overarching  
500 structures and diurnal patterns of both PBLH and cloud distributions, they demonstrate  
501 notable underestimation of PBL-coupled clouds in regions prone to intense convective  
502 activities like GOAMAZON and CACTI. A recurrent theme across our analyses  
503 pinpointed the models' systematic underestimation of boundary layer humidity and its  
504 consequential impact on the formation of coupled clouds. The results also demonstrate  
505 that these biases in GSRMs are intimately associated with the models' tendency to  
506 underestimate boundary layer humidity and the convective initiation within different  
507 ranges of PBL heights.

508 Through detailed intercomparisons with field observations, several models, such as

509 SCREAM, UM, and IFS, demonstrate closer alignment with observed coupled cloud  
510 frequencies and behaviors, while others presented relatively larger discrepancies,  
511 especially in simulating the occurrence of coupled clouds in a high PBLH scenario.

512 Decoupled clouds demonstrate a relatively good agreement between observations and  
513 GSRMs. However, decoupled clouds are also underestimated over the SGP at the high-  
514 level, especially for SCREAM. For GOAMAZON and CACTI, observations suggest a  
515 dominance of PBL-coupled clouds in the low cloud regime, whereas GSRMs tend to  
516 classify a substantial portion of these clouds as decoupled.

517 The underrepresentation of coupled clouds in terms of vertical fraction and  
518 frequency in GSRMs, especially for GOAMAZON and CACTI, underscores the critical  
519 need for model refinement. These findings also shed light on the substantial variability  
520 in capturing cloud-PBL interactions across various GSRMs, highlighting a pervasive  
521 challenge in simulating the complex feedback loops between the land surface, the PBL,  
522 and cloud formation. This challenge is further compounded when considering the  
523 resolution of mountainous terrain features, where even kilometer-scale GSRMs may  
524 fall short. The accurate representation of PBL and PBL moisture emerges as two key  
525 factors for realistic coupled cloud simulations, necessitating a concerted effort toward  
526 honing model parameterizations of these essential processes.

527 GSRMs offer a fine spatial resolution that promises deeper insights into PBL  
528 processes and their complex interactions with convective systems, despite some notable  
529 differences between model and observations. The application of advanced deep  
530 learning techniques presents a promising avenue to bridge the divide between high-

531 resolution models and field observations for cloud simulations (Su and Zhang, 2024).  
532 By enhancing GSRMs with the capabilities to more accurately mimic detailed local-  
533 scale PBL processes and convective systems, this tool can be used for investigating the  
534 evolution of PBL-coupled and decoupled clouds under climate change, offering a robust  
535 platform for exploring the evolution of the Earth's climate system.

536

537 **Acknowledgements:** Work at LLNL is performed under the auspices of the U.S. DOE  
538 by Lawrence Livermore National Laboratory under Contract DE-AC52-07NA27344.  
539 This research used resources of the National Energy Research Scientific Computing  
540 Center (NERSC), a U.S. Department of Energy Office of Science User Facility located  
541 at Lawrence Berkeley National Laboratory, operated under Contract No. DE-AC02-  
542 05CH11231. We acknowledge the U.S. Department of Energy's ARM program for  
543 offering the comprehensive field observations.

544

545 **Data Availability Statement:** ARM radiosonde data, surface fluxes, and cloud masks  
546 are available at [https://adc.arm.gov/discovery/#/results/instrument\\_class::armbe](https://adc.arm.gov/discovery/#/results/instrument_class::armbe).  
547 The data of planetary boundary layer can be downloaded from  
548 <https://www.arm.gov/data/data-sources/pblht-206>. ERA-5 reanalysis data are obtained  
549 from <https://cds.climate.copernicus.eu/cdsapp#!/dataset/reanalysis-era5-pressure-levels?tab=form>. The Global Storm Resolving Models output used in this study is  
550 publicly available as part of the DYAMOND2 intercomparison as described at  
551 <https://www.esiwace.eu/services/dyamond>.

553

554 **References**

- 555 Berg, L. K., and Kassianov, E.I. (2008): Temporal variability of fair-weather cumulus  
 556 statistics at the ACRF SGP site. *J. Climate*, 21(13), 3344–3358.
- 557 Betts, A.K. (2009). Land - surface - atmosphere coupling in observations and models.  
 558 *Journal of Advances in Modeling Earth Systems*, 1(3).
- 559 Bretherton, C. S., Blossey, P. N., and Uchida, J. (2007): Cloud droplet sedimentation,  
 560 entrainment efficiency, and subtropical stratocumulus albedo. *Geophys. Res. Lett.*,  
 561 34(3), L03813.
- 562 Bubnová, R., Hello, G., Bénard, P., & Geleyn, J. F. (1995). Integration of the fully  
 563 elastic equations cast in the hydrostatic pressure terrain-following coordinate in the  
 564 framework of the ARPEGE/Aladin NWP system. *Monthly weather review*, 123(2),  
 565 515-535.
- 566 Caldwell, P.M., Terai, C.R., Hillman, B., Keen, N.D., Bogenschutz, P., Lin, W.,  
 567 Beydoun, H., Taylor, M., Bertagna, L., Bradley, A.M. and Clevenger, T.C., 2021.  
 568 Convection - permitting simulations with the E3SM global atmosphere model.  
 569 *Journal of Advances in Modeling Earth Systems*, 13(11), p.e2021MS002544.
- 570 Clothiaux, E.E., Ackerman, T.P., Mace, G.G., Moran, K.P., Marchand, R.T., Miller,  
 571 M.A. and Martner, B.E., 2000. Objective determination of cloud heights and radar  
 572 reflectivities using a combination of active remote sensors at the ARM CART sites.  
 573 *Journal of Applied Meteorology and Climatology*, 39(5), pp.645-665.
- 574 Clothiaux, E.E., Miller, M.A., Perez, R.C., Turner, D.D., Moran, K.P., Martner, B.E.,  
 575 Ackerman, T.P., Mace, G.G., Marchand, R.T., Widener, K.B. and Rodriguez, D.J.,  
 576 2001. The ARM millimeter wave cloud radars (MMCRs) and the active remote  
 577 sensing of clouds (ARSCL) value added product (VAP) (No. DOE/SC-ARM/VAP-  
 578 002.1). DOE Office of Science Atmospheric Radiation Measurement (ARM)  
 579 Program (United States).
- 580 Cook, D.R., 2018. Energy balance bowen ratio station (EBBR) instrument handbook  
 581 (No. DOE/SC-ARM/TR-037). DOE Office of Science Atmospheric Radiation  
 582 Measurement (ARM) Program (United States).
- 583 Fast, J.D., Berg, L.K., Alexander, L., Bell, D., D'Ambro, E., Hubbe, J., Kuang, C., Liu,  
 584 J., Long, C., Matthews, A. and Mei, F., 2019b. Overview of the HI-SCALE field  
 585 campaign: A new perspective on shallow convective clouds. *Bulletin of the  
 586 American Meteorological Society*, 100(5), pp.821-840.
- 587 Fast, J.D., Berg, L.K., Feng, Z., Mei, F., Newsom, R., Sakaguchi, K. and Xiao, H.,  
 588 2019a. The impact of variable land - atmosphere coupling on convective cloud  
 589 populations observed during the 2016 HI - SCALE field campaign. *Journal of  
 590 Advances in Modeling Earth Systems*, 11(8), pp.2629-2654.
- 591 Gelaro, R., McCarty, W., Suárez, M.J., Todling, R., Molod, A., Takacs, L., Randles,  
 592 C.A., Darmenov, A., Bosilovich, M.G., Reichle, R. and Wargan, K., 2017. The  
 593 modern-era retrospective analysis for research and applications, version 2  
 594 (MERRA-2). *Journal of climate*, 30(14), pp.5419-5454.
- 595 Golaz, J.C., Larson, V.E. and Cotton, W.R. (2002). A PDF-based model for boundary  
 596 layer clouds. Part I: Method and model description. *Journal of the atmospheric*

- 597 sciences, 59(24), pp.3540-3551.
- 598 Guo, J., Su, T., Chen, D., Wang, J., Li, Z., Lv, Y., ... & Zhai, P. (2019). Declining  
599 summertime local - scale precipitation frequency over China and the United States,  
600 1981 – 2012: The disparate roles of aerosols. *Geophysical Research Letters*, 46(22),  
601 13281-13289.
- 602 Harris, L., Zhou, L., Lin, S.J., Chen, J.H., Chen, X., Gao, K., Morin, M., Rees, S., Sun,  
603 Y., Tong, M. and Xiang, B., 2020. GFDL SHiELD: A unified system for weather -  
604 to - seasonal prediction. *Journal of Advances in Modeling Earth Systems*, 12(10),  
605 p.e2020MS002223.
- 606 Hersbach, H., Bell, B., Berrisford, P., Hirahara, S., Horányi, A., Muñoz-Sabater, J.,  
607 Nicolas, J., Peubey, C., Radu, R., Schepers, D. and Simmons, A., 2020. The ERA5  
608 global reanalysis. *Quarterly Journal of the Royal Meteorological Society*, 146(730),  
609 pp.1999-2049.
- 610 Hohenegger, C., Korn, P., Linardakis, L., Redler, R., Schnur, R., Adamidis, P., Bao, J.,  
611 Bastin, S., Behravesh, M., Bergemann, M. and Biercamp, J., 2023. ICON-Sapphire:  
612 simulating the components of the Earth system and their interactions at kilometer  
613 and subkilometer scales. *Geoscientific Model Development*, 16(2), pp.779-811.
- 614 Kennedy, A.D., Dong, X. and Xi, B., 2014. Cloud fraction at the ARM SGP site:  
615 instrument and sampling considerations from 14 years of ARSCL. *Theoretical and  
616 applied climatology*, 115, pp.91-105.
- 617 Khairoutdinov, M. F., Blossey, P. N., & Bretherton, C. S. (2022). Global system for  
618 atmospheric modeling: Model description and preliminary results. *Journal of  
619 Advances in Modeling Earth Systems*, 14(6), e2021MS002968.
- 620 Klocke, D., Brueck, M., Hohenegger, C., & Stevens, B. (2017). Rediscovery of the  
621 doldrums in storm-resolving simulations over the tropical Atlantic. *Nature  
622 Geoscience*, 10(12), 891-896.
- 623 Kollias, P., Bharadwaj, N., Clothiaux, E.E., Lamer, K., Oue, M., Hardin, J., Isom, B.,  
624 Lindenmaier, I., Matthews, A., Luke, E.P. and Giangrande, S.E., 2020. The ARM  
625 radar network: At the leading edge of cloud and precipitation observations. *Bulletin  
626 of the American Meteorological Society*, 101(5), pp.E588-E607.
- 627 Lareau, N.P., Zhang, Y. and Klein, S.A. (2018). Observed boundary layer controls on  
628 shallow cumulus at the ARM Southern Great Plains site. *Journal of the Atmospheric  
629 Sciences*, 75(7), pp.2235-2255.
- 630 Lee, J.M., Zhang, Y. and Klein, S.A., 2019. The effect of land surface heterogeneity and  
631 background wind on shallow cumulus clouds and the transition to deeper  
632 convection. *Journal of the Atmospheric Sciences*, 76(2), pp.401-419.
- 633 Lin, Y., Dong, W., Zhang, M., Xie, Y., Xue, W., Huang, J. and Luo, Y., 2017. Causes of  
634 model dry and warm bias over central US and impact on climate projections. *Nature  
635 Communications*, 8(1), p.881.
- 636 Ma, H.Y., Klein, S.A., Xie, S., Zhang, C., Tang, S., Tang, Q., Morcrette, C.J., Van  
637 Weverberg, K., Petch, J., Ahlgrimm, M. and Berg, L.K., 2018. CAUSES: On the  
638 role of surface energy budget errors to the warm surface air temperature error over  
639 the Central United States. *Journal of Geophysical Research: Atmospheres*, 123(5),  
640 pp.2888-2909.

- 641 Malardel, S., Wedi, N., Deconinck, W., Diamantakis, M., Kühnlein, C., Mozdzynski,  
642 G., ... & Smolarkiewicz, P. (2016). A new grid for the IFS. ECMWF newsletter,  
643 146(23-28), 321.
- 644 McTaggart-Cowan, R., Vaillancourt, P. A., Zadra, A., Chamberland, S., Charron, M.,  
645 Corvec, S., ... & Yang, J. (2019). Modernization of atmospheric physics  
646 parameterization in Canadian NWP. Journal of Advances in Modeling Earth  
647 Systems, 11(11), 3593-3635.
- 648 Miao, H., Wang, X., Liu, Y. and Wu, G., 2019. An evaluation of cloud vertical structure  
649 in three reanalyses against CloudSat/cloud - aerosol lidar and infrared pathfinder  
650 satellite observations. Atmospheric Science Letters, 20(7), p.e906.
- 651 Moeng, C.H., Cotton, W.R., Bretherton, C., Chlond, A., Khairoutdinov, M., Krueger,  
652 S., Lewellen, W.S., MacVean, M.K., Pasquier, J.R.M., Rand, H.A. and Siebesma,  
653 A.P. (1996). Simulation of a stratocumulus-topped planetary boundary layer:  
654 Intercomparison among different numerical codes. Bulletin of the American  
655 Meteorological Society, 77(2), pp.261-278.
- 656 Molod, A., Takacs, L., Suarez, M., Bacmeister, J., Song, I.S. and Eichmann, A., 2012.  
657 The GEOS-5 atmospheric general circulation model: Mean climate and  
658 development from MERRA to Fortuna (No. GSFC. TM. 01153.2012).
- 659 Poll, S., Shrestha, P. and Simmer, C. (2022). Grid resolution dependency of land surface  
660 heterogeneity effects on boundary - layer structure. Quarterly Journal of the Royal  
661 Meteorological Society, 148(742), pp.141-158.
- 662 Poll, S., Shrestha, P. and Simmer, C., 2022. Grid resolution dependency of land surface  
663 heterogeneity effects on boundary - layer structure. Quarterly Journal of the Royal  
664 Meteorological Society, 148(742), pp.141-158.
- 665 Qian, Y., Guo, Z., Larson, V.E., Leung, L.R., Lin, W., Ma, P.L., Wan, H., Wang, H.,  
666 Xiao, H., Xie, S. and Yang, B., 2023. Region and cloud regime dependence of  
667 parametric sensitivity in E3SM atmosphere model. Climate Dynamics, pp.1-17.
- 668 Qin, H., Klein, S. A., Ma, H. Y., Van Weverberg, K., Feng, Z., Chen, X., ... & Webster,  
669 S. (2023). Summertime Near - Surface Temperature Biases Over the Central United  
670 States in Convection - Permitting Simulations. Journal of Geophysical Research: Atmospheres, 128(22), e2023JD038624.
- 672 Randles, C.A., Da Silva, A.M., Buchard, V., Colarco, P.R., Darmenov, A., Govindaraju,  
673 R., Smirnov, A., Holben, B., Ferrare, R., Hair, J. and Shinozuka, Y., 2017. The  
674 MERRA-2 aerosol reanalysis, 1980 onward. Part I: System description and data  
675 assimilation evaluation. Journal of climate, 30(17), pp.6823-6850.
- 676 Rieck, M., Hohenegger, C. and van Heerwaarden, C.C., 2014. The influence of land  
677 surface heterogeneities on cloud size development. Monthly Weather Review,  
678 142(10), pp.3830-3846.
- 679 Roberts, C. D., Senan, R., Molteni, F., Boussutta, S., Mayer, M., & Keeley, S. P. (2018).  
680 Climate model configurations of the ECMWF Integrated Forecasting System  
681 (ECMWF-IFS cycle 43r1) for HighResMIP. Geoscientific model development,  
682 11(9), 3681-3712.
- 683 Romps, D.M. (2017). Exact expression for the lifting condensation level. Journal of the  
684 Atmospheric Sciences, 74(12), pp.3891-3900.

- 685 Sakaguchi, K., Berg, L.K., Chen, J., Fast, J., Newsom, R., Tai, S.L., Yang, Z., Gustafson  
686 Jr, W.I., Gaudet, B.J., Huang, M. and Pekour, M., 2022. Determining spatial scales  
687 of soil moisture—Cloud coupling pathways using semi - idealized simulations.  
688 *Journal of Geophysical Research: Atmospheres*, 127(2), p.e2021JD035282.
- 689 Satoh, M., Tomita, H., Miura, H., Iga, S., and Nasuno, T, 2005. Development of a global  
690 cloud resolving model – a multi-scale structure of tropical convections, *J. Earth  
691 Simulator*, 3, 11–19.
- 692 Schneider, T., Kaul, C.M. and Pressel, K.G., 2019. Possible climate transitions from  
693 breakup of stratocumulus decks under greenhouse warming. *Nature Geoscience*,  
694 12(3), pp.163-167.
- 695 Stevens, B., Satoh, M., Auger, L., Biercamp, J., Bretherton, C. S., Chen, X., ... & Zhou,  
696 L. (2019). DYAMOND: the DYnamics of the Atmospheric general circulation  
697 Modeled On Non-hydrostatic Domains. *Progress in Earth and Planetary Science*,  
698 6(1), 1-17.
- 699 Su, T. et al. (2024). Observation and Reanalysis Derived Relationships Between Cloud  
700 and Land Surface Fluxes Across Cumulus and Stratiform Coupling Over the  
701 Southern Great Plains. *Geophysical Research Letters* (In Press)
- 702 Su, T., Li, Z. and Zheng, Y. (2023). Cloud - Surface Coupling Alters the Morning  
703 Transition From Stable to Unstable Boundary Layer. *Geophysical Research Letters*,  
704 50(5), p.e2022GL102256.
- 705 Su, T., Li, Z., Zheng, Y., Wu, T., Wu, H., & Guo, J. (2022a). Aerosol-boundary layer  
706 interaction modulated entrainment process. *npj Climate and Atmospheric Science*,  
707 5(1), 64.
- 708 Su, T., Zheng, Y., & Li, Z. (2022b). Methodology to determine the coupling of  
709 continental clouds with surface and boundary layer height under cloudy conditions  
710 from lidar and meteorological data. *Atmospheric Chemistry and Physics*, 22(2),  
711 1453-1466.
- 712 Tang, Q., Klein, S.A., Xie, S., Lin, W., Golaz, J.C., Roesler, E.L., Taylor, M.A., Rasch,  
713 P.J., Bader, D.C., Berg, L.K. and Caldwell, P., 2019. Regionally refined test bed in  
714 E3SM atmosphere model version 1 (EAMv1) and applications for high-resolution  
715 modeling. *Geoscientific Model Development*, 12(7), pp.2679-2706.
- 716 Tao, C., Zhang, Y., Tang, Q., Ma, H.Y., Ghate, V.P., Tang, S., Xie, S. and Santanello,  
717 J.A., 2021. Land–Atmosphere coupling at the US Southern Great Plains: A  
718 comparison on local convective regimes between ARM observations, reanalysis,  
719 and climate model simulations. *Journal of Hydrometeorology*, 22(2), pp.463-481.
- 720 Tao, C., Zhang, Y., Tang, S., Tang, Q., Ma, H.Y., Xie, S. and Zhang, M., 2019. Regional  
721 moisture budget and land - atmosphere coupling over the US Southern Great Plains  
722 inferred from the ARM long - term observations. *Journal of Geophysical Research:  
723 Atmospheres*, 124(17-18), pp.10091-10108.
- 724 Teixeira, J., and Hogan, T. F. (2002): Boundary layer clouds in a global atmospheric  
725 model: simple cloud cover parameterizations. *J. Climate*, 15(11), 1261–1276.
- 726 Tian, J., Zhang, Y., Klein, S.A., Öktem, R. and Wang, L., 2022. How does land cover  
727 and its heterogeneity length scales affect the formation of summertime shallow  
728 cumulus clouds in observations from the US Southern Great Plains?. *Geophysical*

- 729 Research Letters, 49(7), p.e2021GL097070.
- 730 Tian, J., Zhang, Y., Klein, S.A., Wang, L., Öktem, R. and Romps, D.M., 2021.  
731 Summertime continental shallow cumulus cloud detection using GOES-16 satellite  
732 and ground-based stereo cameras at the DOE ARM Southern Great Plains site.  
733 Remote Sensing, 13(12), p.2309.
- 734 Tiedtke, M., 1993. Representation of clouds in large-scale models. Monthly Weather  
735 Review, 121(11), pp.3040-3061.
- 736 Walters, D., Baran, A.J., Boutle, I., Brooks, M., Earnshaw, P., Edwards, J., Furtado, K.,  
737 Hill, P., Lock, A., Manners, J. and Morcrette, C., 2019. The Met Office Unified  
738 Model global atmosphere 7.0/7.1 and JULES global land 7.0 configurations.  
739 Geoscientific Model Development, 12(5), pp.1909-1963.
- 740 Xian, T., Guo, J., Zhao, R., Su, T. and Li, Z., 2023. The impact of urbanization on  
741 mesoscale convective systems in the Yangtze River Delta region of China: insights  
742 gained from observations and modeling. Journal of Geophysical Research: Atmospheres,  
743 128(3), p.e2022JD037709.
- 744 Xiao, H., Berg, L.K. and Huang, M., 2018. The impact of surface heterogeneities and  
745 land - atmosphere interactions on shallow clouds over ARM SGP site. Journal of  
746 Advances in Modeling Earth Systems, 10(6), pp.1220-1244.
- 747 Xie, S., McCoy, R.B., Klein, S.A., Cederwall, R.T., Wiscombe, W.J., Clothiaux, E.E.,  
748 Gaustad, K.L., Golaz, J.C., Hall, S.D., Jensen, M.P. and Johnson, K.L., 2010.  
749 Clouds and more: ARM climate modeling best estimate data: A new data product  
750 for climate studies. Bulletin of the American Meteorological Society, 91(LLNL-  
751 JRNL-412676).
- 752 Zängl, G., Reinert, D., Rípodas, P. and Baldauf, M., 2015. The ICON (ICOahedral  
753 Non - hydrostatic) modelling framework of DWD and MPI - M: Description of the  
754 non - hydrostatic dynamical core. Quarterly Journal of the Royal Meteorological  
755 Society, 141(687), pp.563-579.
- 756 Zhang, M., Wang, X., Chen, J., Cheng, T., Wang, T., Yang, X., Gong, Y., Geng, F. and  
757 Chen, C. (2010). Physical characterization of aerosol particles during the Chinese  
758 New Year's firework events. Atmospheric Environment, 44(39), pp.5191-5198.
- 759 Zhang, Y. and Klein, S.A. (2010). Mechanisms affecting the transition from shallow to  
760 deep convection over land: Inferences from observations of the diurnal cycle  
761 collected at the ARM Southern Great Plains site. Journal of the Atmospheric  
762 Sciences, 67(9), pp.2943-2959.
- 763 Zhang, Y. and Klein, S.A., 2013. Factors controlling the vertical extent of fair-weather  
764 shallow cumulus clouds over land: Investigation of diurnal-cycle observations  
765 collected at the ARM Southern Great Plains site. Journal of the Atmospheric  
766 Sciences, 70(4), pp.1297-1315.
- 767 Zhang, Y., Klein, S.A., Fan, J., Chandra, A.S., Kollias, P., Xie, S. and Tang, S., 2017.  
768 Large-eddy simulation of shallow cumulus over land: A composite case based on  
769 ARM long-term observations at its Southern Great Plains site. Journal of the  
770 Atmospheric Sciences, 74(10), pp.3229-3251.
- 771 Zheng, Y., Zhang, H., Rosenfeld, D., Lee, S.S., Su, T. and Li, Z. (2021). Idealized large-  
772 eddy simulations of stratocumulus advecting over cold water. Part I: Boundary layer

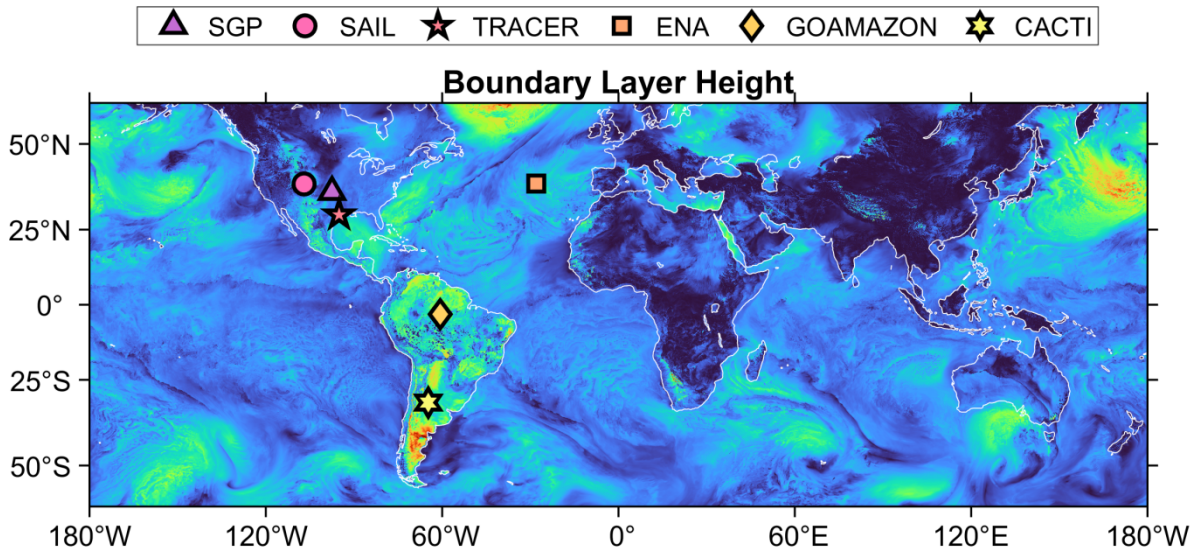
773 decoupling. *Journal of the Atmospheric Sciences*, 78(12), pp.4089-4102.

774 **Table**

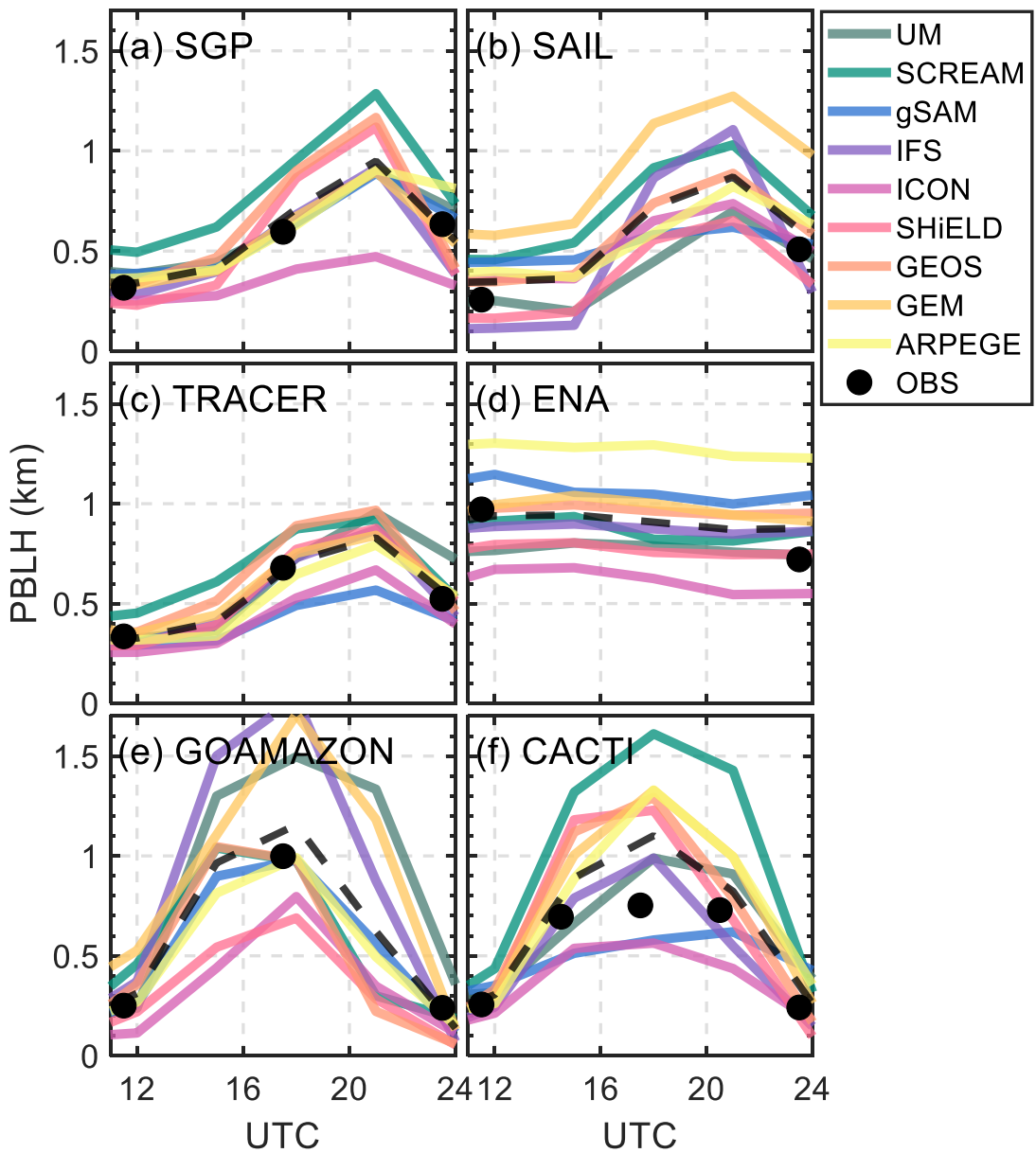
775 **Table 1:** Overview of Global Storm-Resolving Models (GSRMs) Utilized in the Study,  
 776 Detailing Model Names, Their Respective Horizontal Grid Spacings, and Affiliated  
 777 Institutions.

<b>Model Name</b>	<b>Horizontal Grid (km)</b>	<b>Institution</b>	<b>Reference</b>
GEOS	3.0	NASA's Goddard Space Flight Center (NASA/GSFC), USA	Molod et al. 2012
ICON	5.0	Max Planck Institute for Meteorology (MPI-MET),	Zängl et al. 2015
SCREAM	3.25	Lawrence Livermore National Laboratory (LLNL), USA	Caldwell et al. 2021
SHiELD	3.0	National Oceanic and Atmospheric Administration (NOAA), USA	Harris et al. 2020
UM	4.8	National Centre for Atmospheric Science (NCAS), UK	Walters et al. 2019
gSAM	4.0	Stony Brook University (SBU), USA	Khairoutdinov et al. 2022
IFS	4.0	European Centre for Medium-Range Weather Forecasts (ECMWF), EU	Malardel et al. 2016
GEM	5.0	Environment and Climate Change Canada (ECCC)	McTaggart-Cowan et al. 2019
ARPEGE	2.5	Météo-France, FR	Bubnová et al. 1995

778

779 **Figures**

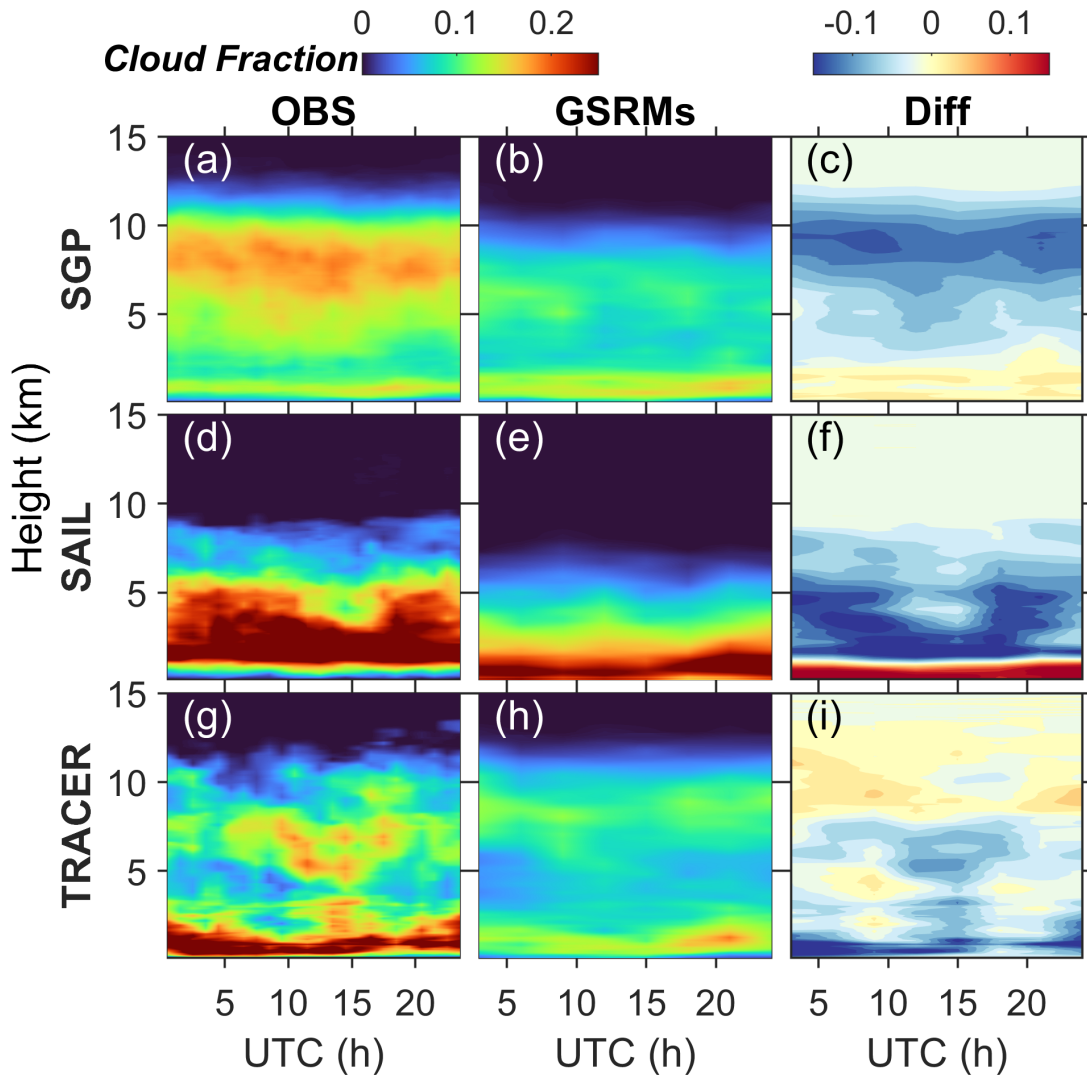
780  
781 **Figure 1.** Global map depicting the Planetary Boundary Layer Height (PBLH) as  
782 simulated by the ECWMF IFS-4km on January 22, 2020, at 18:00 UTC. The color scale  
783 represents the height of the atmospheric boundary layer, with darker regions indicating  
784 lower heights and lighter regions higher heights. The six field campaign sites used for  
785 model evaluation are marked with distinct symbols: SGP (triangle), SAIL (circle),  
786 TRACER (star), ENA (square), GOAMAZON (diamond), and CACTI (pentagon).



787

788 **Figure 2:** Diurnal variations in the planetary boundary layer height (PBLH) across  
 789 different geographical regions as captured by various Global Storm-Resolving Models  
 790 (GSRMs) and compared to field observations (OBS). Each panel represents different  
 791 sites: (a) SGP, (b) SAIL, (c) TRACER, (d) ENA, (e) GOAMAZON, and (f) CACTI.  
 792 The colored lines correspond to the PBLH predicted by each model, including UM,  
 793 SCREAM, g SAM, IFS, ICON, SHIELD, GEOS, GEM, and ARPEGE, illustrating the  
 794 range of simulation outputs across models. Black dots represent observed PBLH values,  
 795 serving as a reference for evaluating model performance.

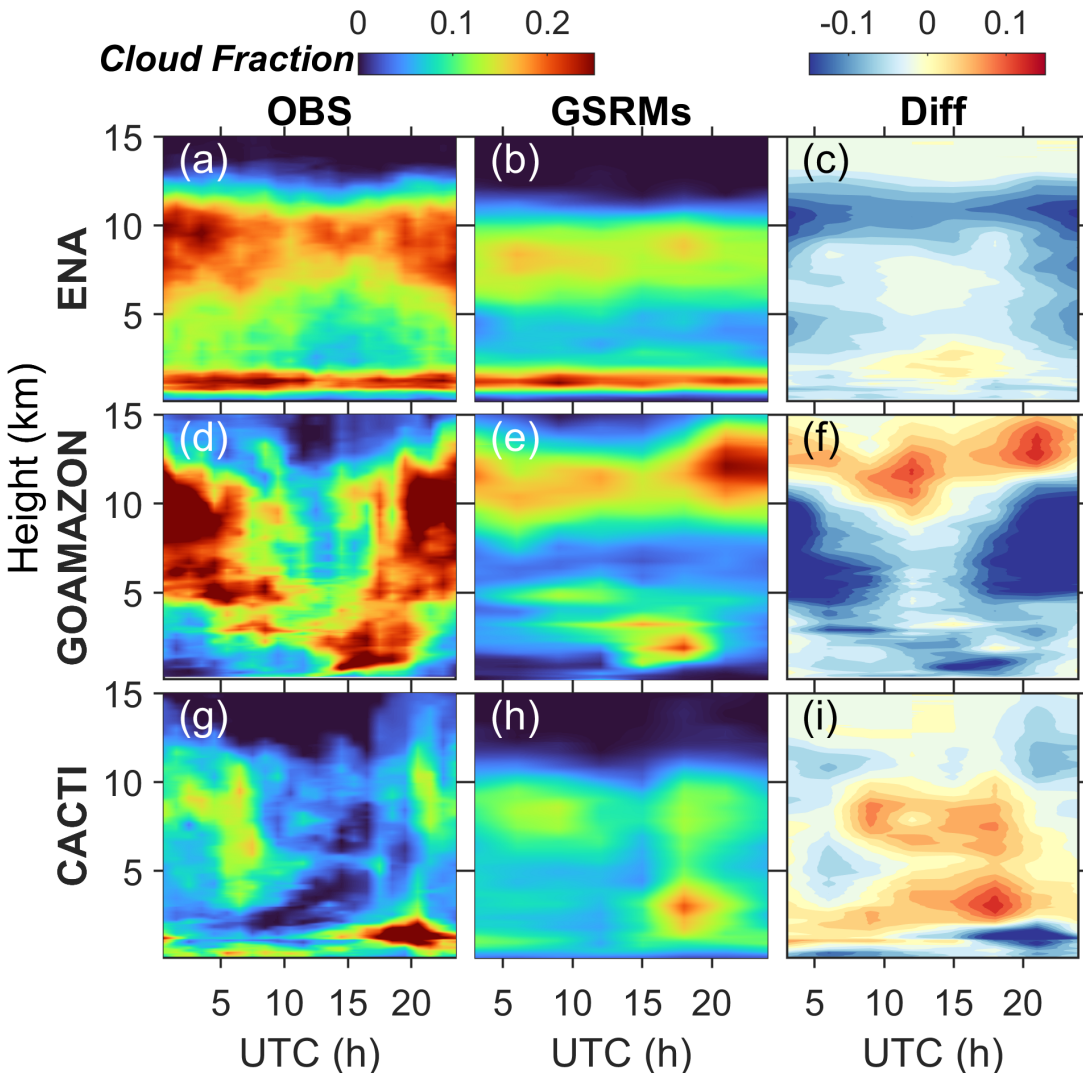
796



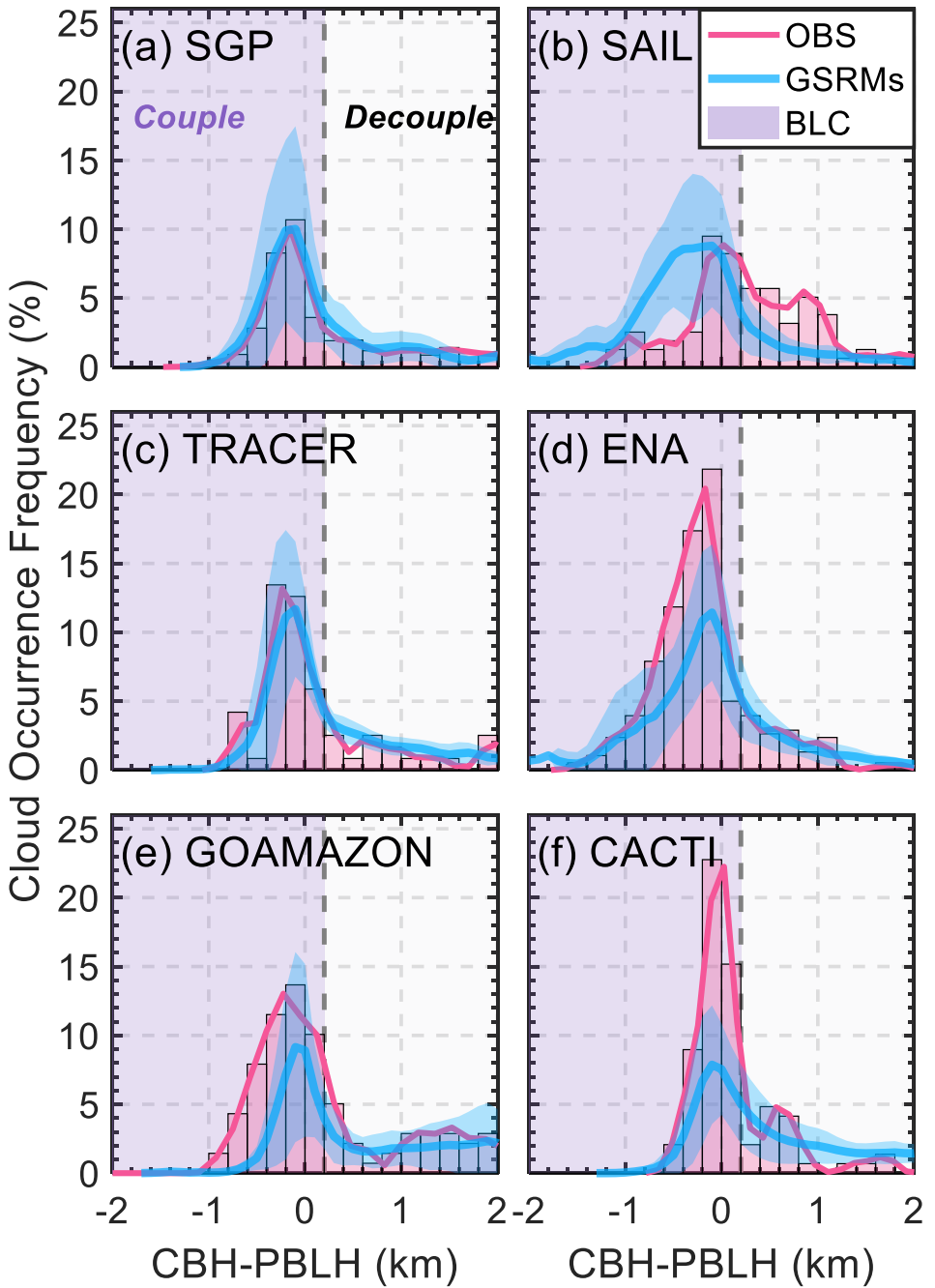
797

798

**Figure 3.** Diurnal variation of cloud fraction profiles at different atmospheric heights, contrasting observational data (OBS) with ensemble mean predictions from Global Storm-Resolving Models (GSRMs) alongside their respective differences. The first column (a, d, g) shows the observed cloud fraction over the course of the day at the SGP, SAIL, and TRACER sites, respectively. The second column (b, e, h) illustrates the corresponding ensemble mean cloud fraction from GSRMs. The third column (c, f, i) exhibits the difference (Diff) between the GSRM ensemble mean and observations.

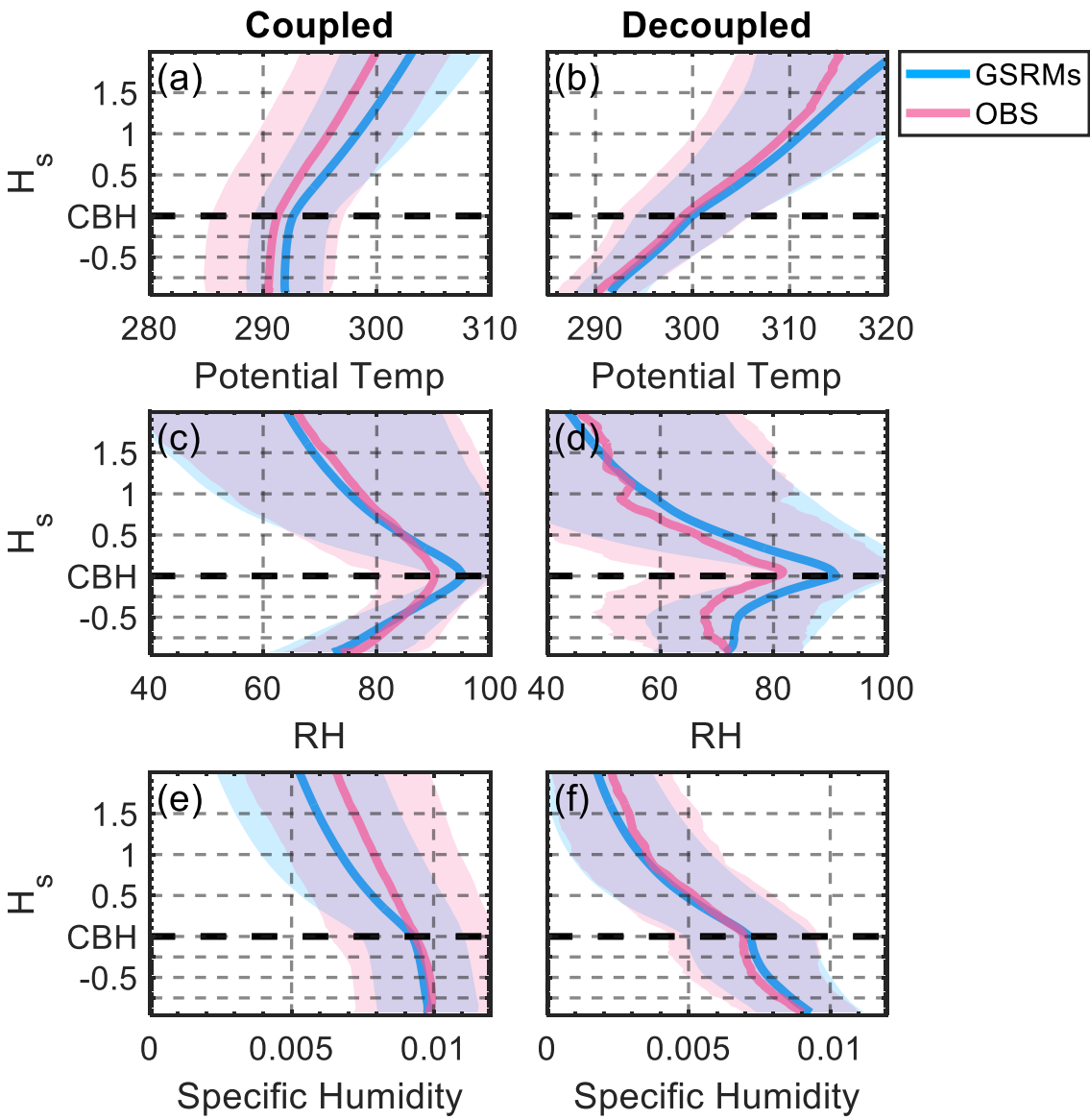


805  
806 **Figure 4.** Diurnal variation of cloud fraction profiles at different atmospheric heights,  
807 contrasting observational data (OBS) with ensemble mean predictions from Global  
808 Storm-Resolving Models (GSRMs) alongside their respective differences. The first  
809 column (a, d, g) shows the observed cloud fraction over the course of the day at the  
810 ENA, GOAMAZON, and CACTI sites, respectively. The second column (b, e, h)  
811 illustrates the corresponding ensemble mean cloud fraction from GSRMs. The third  
812 column (c, f, i) exhibits the difference (Diff) between the GSRM ensemble mean and  
813 observations.



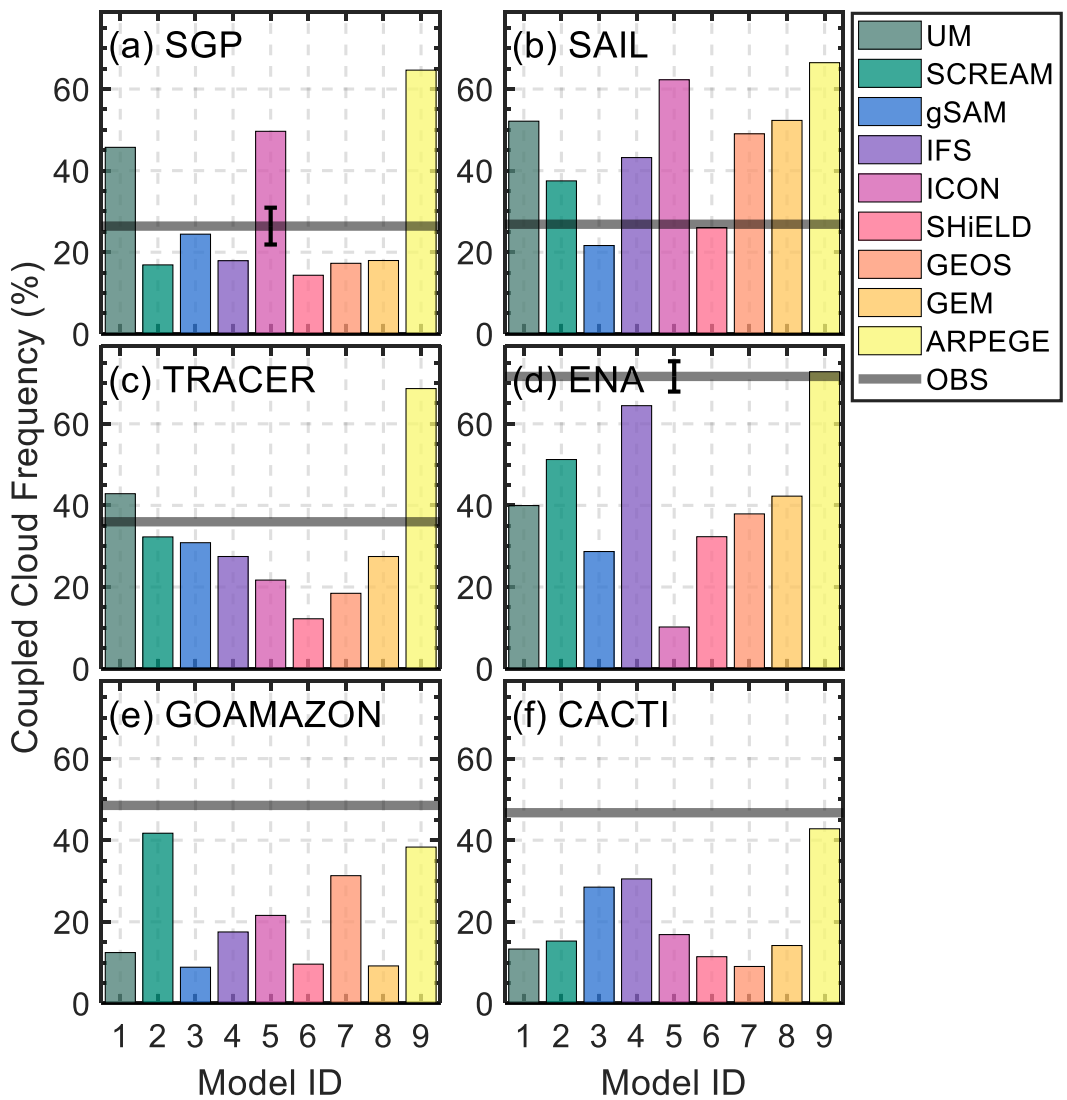
814

815 **Figure 5.** The distribution of cloud occurrence as a function of the difference between  
 816 cloud base height (CBH) and PBLH across different observational and modeling studies.  
 817 Panels (a) through (f) represent different field campaigns: SGP, SAIL, TRACER, ENA,  
 818 GOAMAZON, and CACTI, respectively. Observational data (OBS) are shown in red,  
 819 while outputs from Global Storm-Resolving Models (GSRMs) are presented in blue,  
 820 with the shaded blue area indicating the standard deviation among different GSRMs.  
 821 The vertical dashed lines delineate the transition from coupled (left) to decoupled (right)  
 822 boundary layer states.



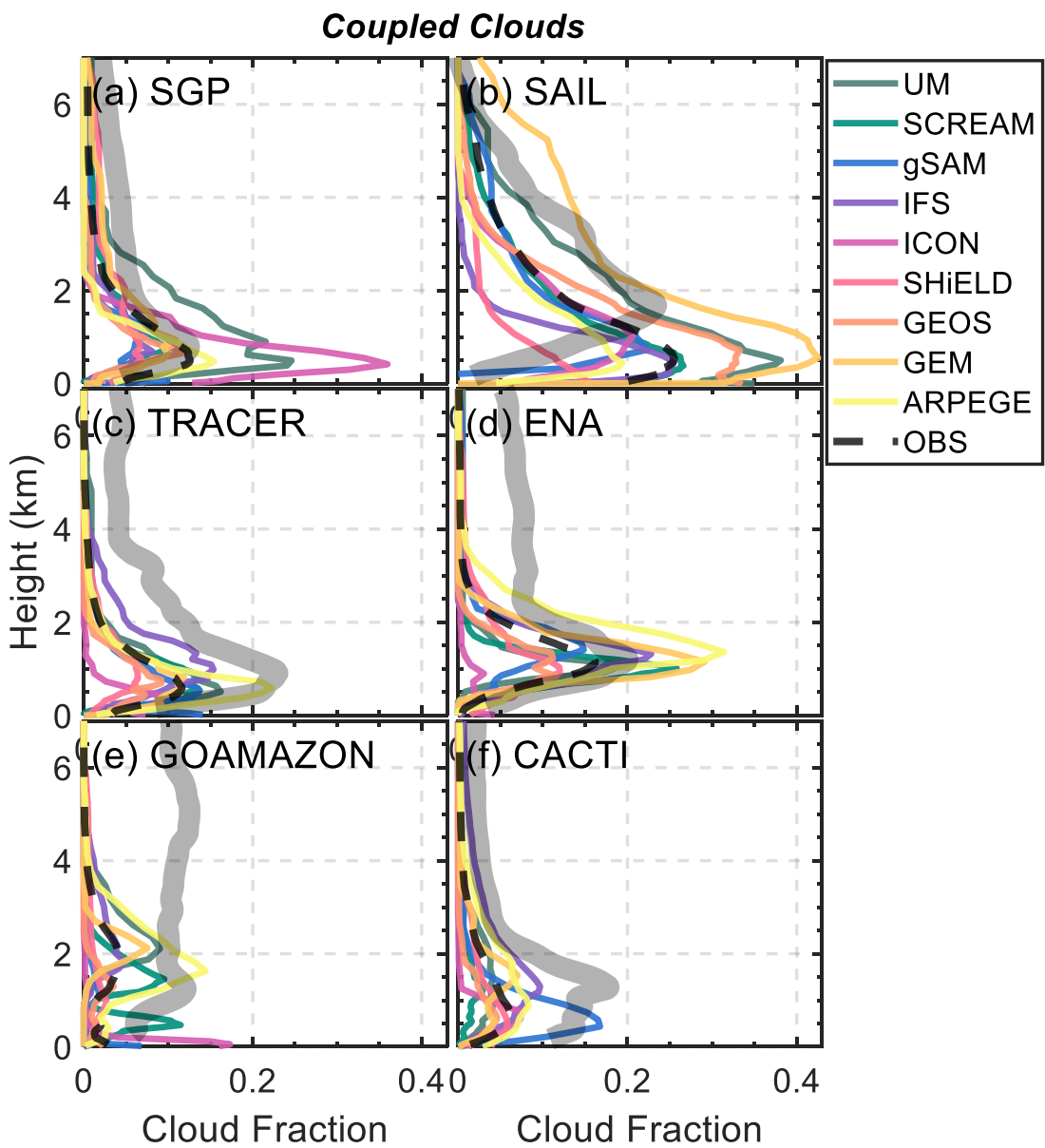
823

824 **Figure 6.** Profiles of coupled (left column) and decoupled (right column) clouds as  
 825 represented by Global Storm-Resolving Models (GSRMs, blue lines) and field  
 826 observations (OBS, red lines) for (a, b) potential temperature, (c, d) relative humidity  
 827 (RH), and (e, f) specific humidity. The vertical scale,  $H_s$ , represents the normalized  
 828 height, calculated as the ratio of altitude to the cloud base height (CBH, denoted by the  
 829 dashed black line). The shaded regions around these lines illustrate the standard  
 830 deviations, indicating the variability within the GSRM outputs and observational data.

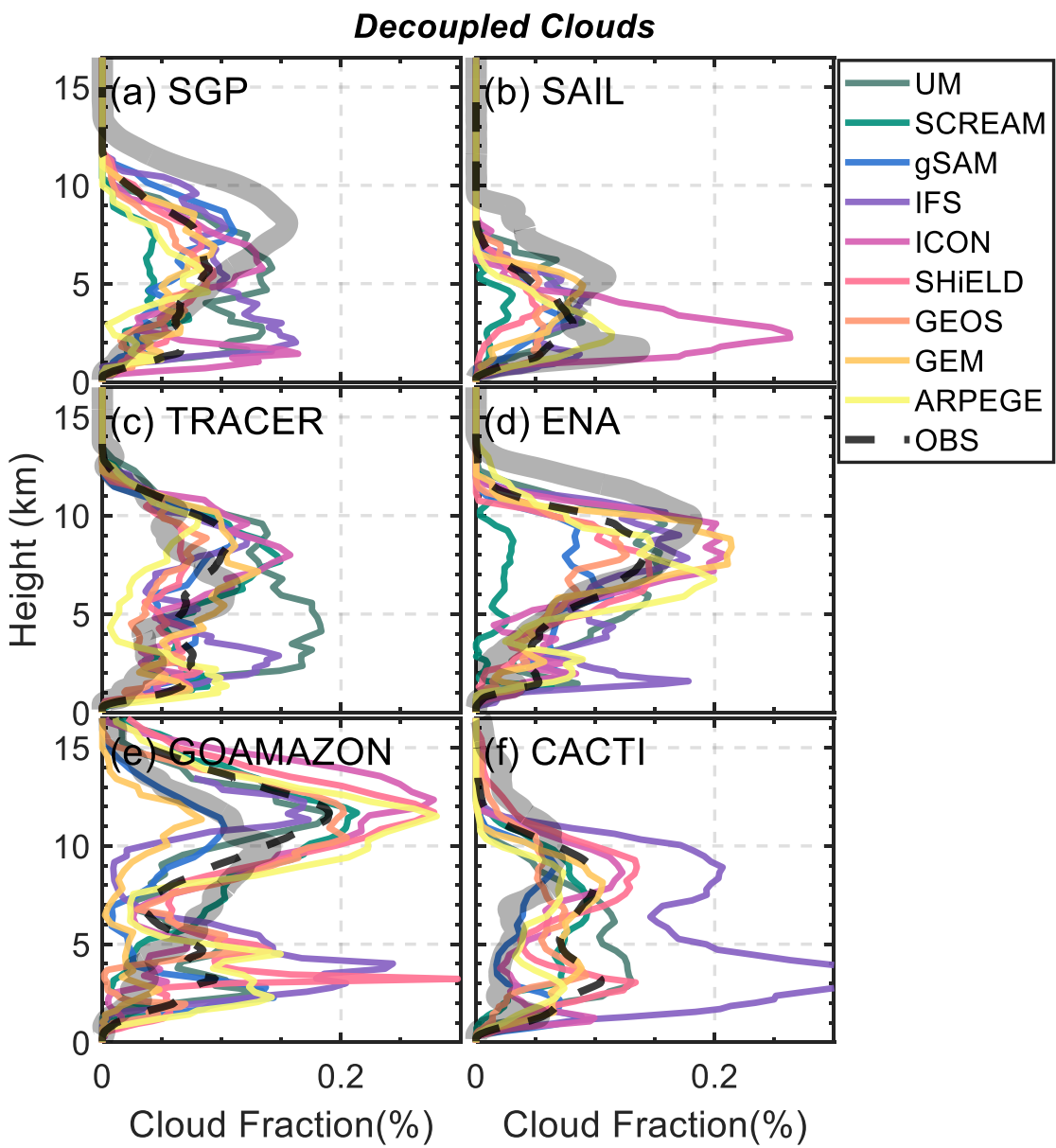


831

832 **Figure 7.** Comparison of boundary-layer-coupled cloud frequency as observed in field  
 833 campaigns (indicated by the red line) against frequencies derived from various Global  
 834 Storm-Resolving Models (GSRMs). Each panel represents cloud frequency data for a  
 835 different geographical site: (a) SGP, (b) SAIL, (c) TRACER, (d) ENA, (e)  
 836 GOAMAZON, and (f) CACTI. The colored bars correspond to different GSRMs as  
 837 denoted in the legend, with the Model IDs on the x-axis representing UM, SCREAM,  
 838 gSAM, IFS, ICON, SHIELD, GEOS, GEM, and ARPEGE respectively. In (a, d), the  
 839 error bars indicate the standard deviations for the values of different year  
 840

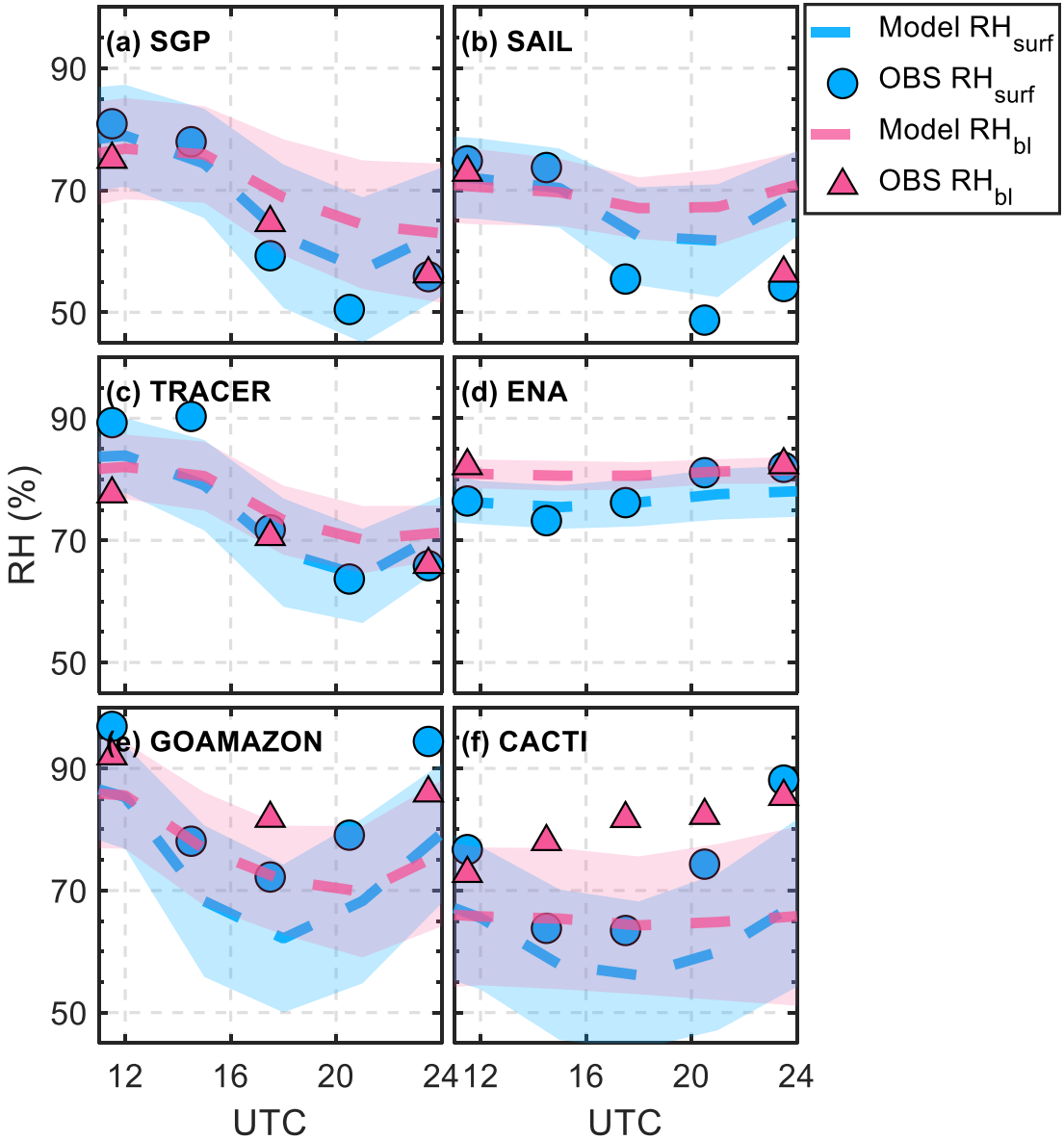


841  
 842 **Figure 8.** Vertical profiles of coupled cloud fraction as simulated by individual Global  
 843 Storm-Resolving Models (GSRMs) compared to field observations for six sites: (a) SGP,  
 844 (b) SAIL, (c) TRACER, (d) ENA, (e) GOAMAZON, and (f) CACTI. The grey line  
 845 represents observed cloud fractions, while the colored lines correspond to the cloud  
 846 fraction profiles from different GSRMs, with each color representing a different model  
 847 as outlined in the legend (UM, SCREAM, gSAM, IFS, ICON, SHIELD, GEOS, GEM,  
 848 and ARPEGE).

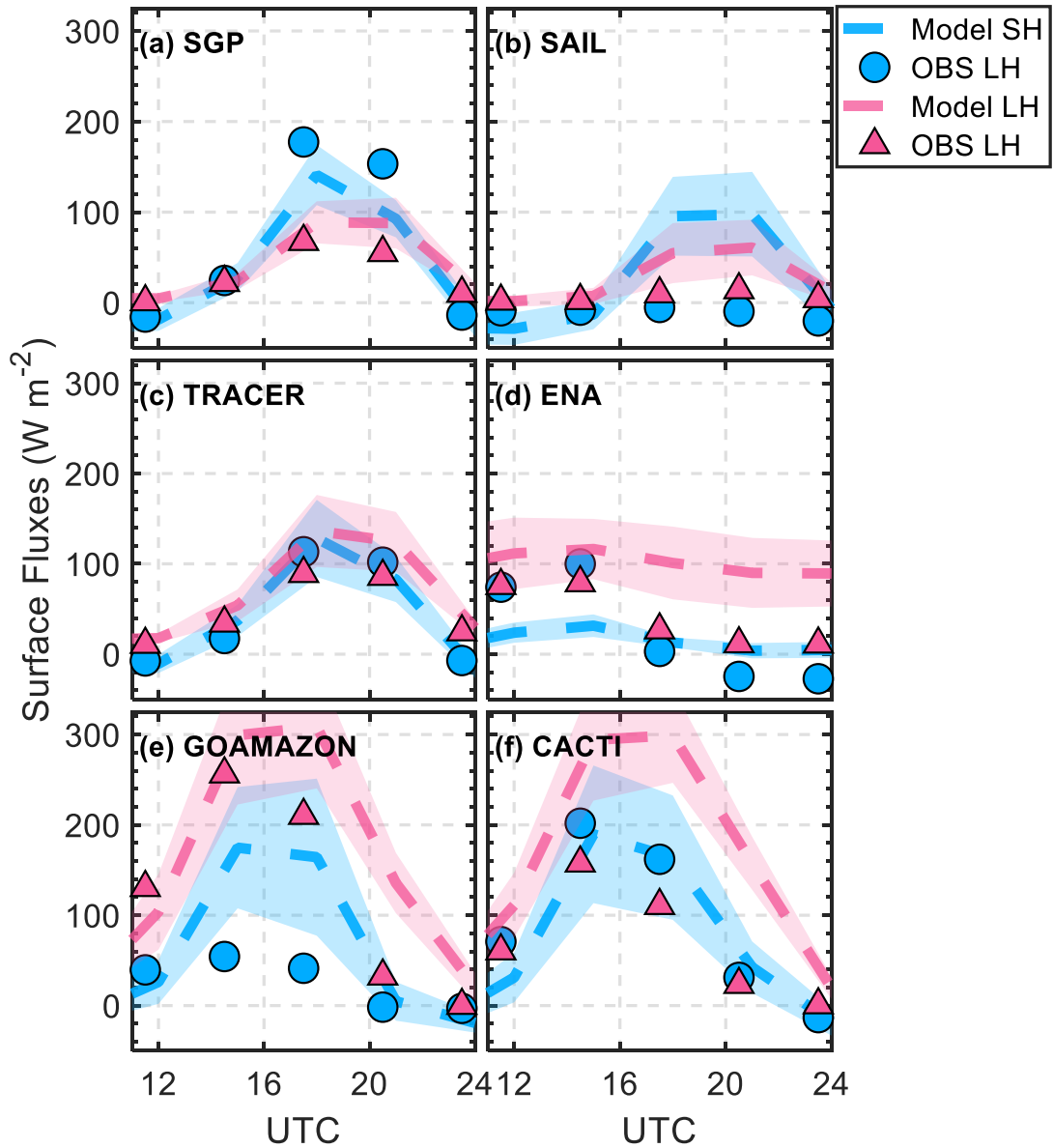


849  
850 **Figure 9.** Vertical profiles of decoupled cloud fraction as simulated by individual  
851 Global Storm-Resolving Models (GSRMs) compared to field observations for six sites:  
852 (a) SGP, (b) SAIL, (c) TRACER, (d) ENA, (e) GOAMAZON, and (f) CACTI. The grey  
853 line represents observed cloud fractions, while the colored lines correspond to the cloud  
854 fraction profiles from different GSRMs, with each color representing a different model  
855 as outlined in the legend (UM, SCREAM, gSAM, IFS, ICON, SHIELD, GEOS, GEM,  
856 and ARPEGE).

857  
858  
859

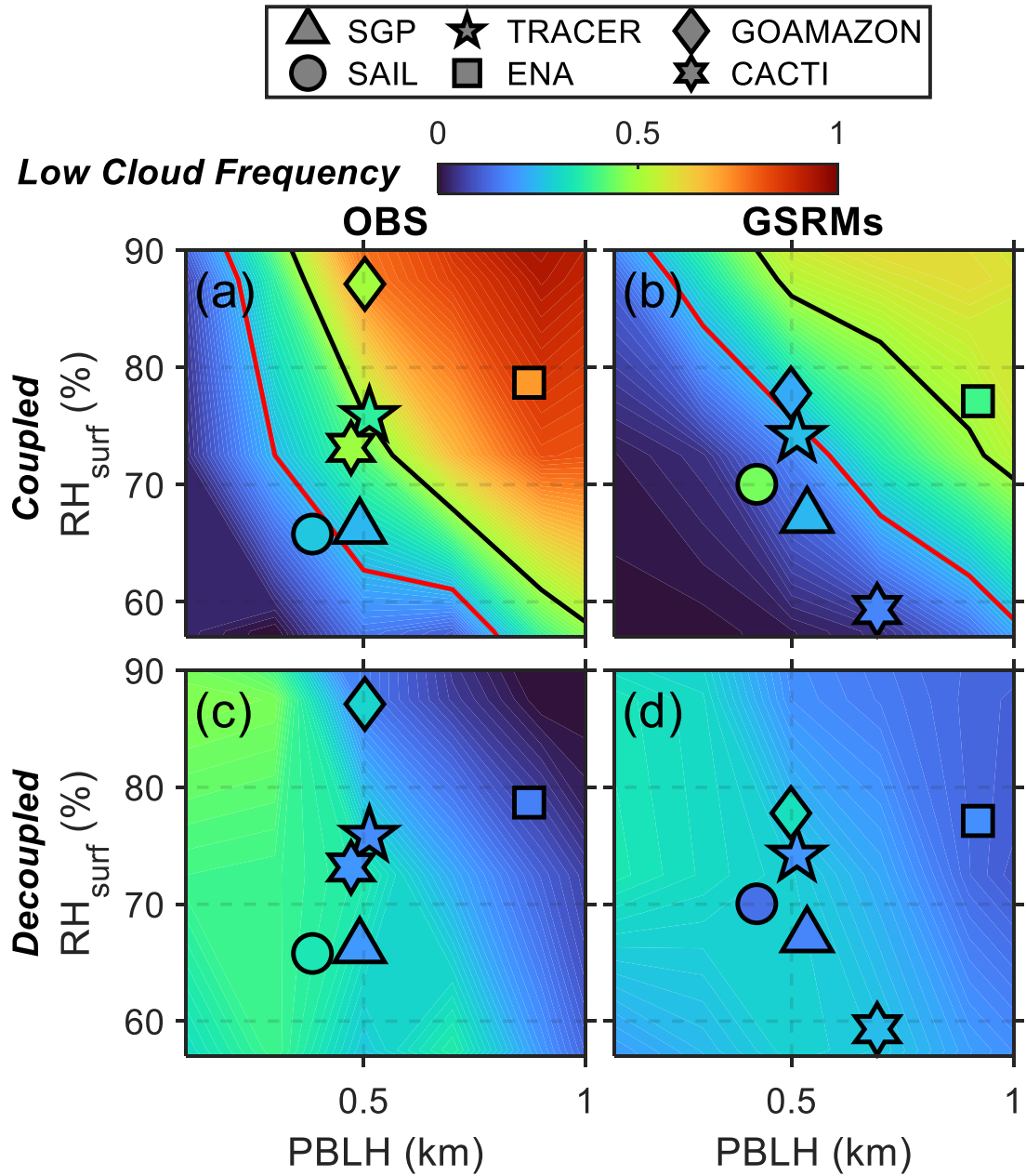


860  
 861 **Figure 10.** Diurnal variations in surface RH ( $RH_{surf}$ , blue) and mean RH within  
 862 boundary layer ( $RH_{bl}$ , red) across six geographical regions, as produced by various  
 863 Global Storm-Resolving Models (GSRMs) and compared to field observations (OBS).  
 864 Each panel corresponds to a different site: (a) SGP, (b) SAIL, (c) TRACER, (d) ENA,  
 865 (e) GOAMAZON, and (f) CACTI. Solid lines indicate the mean values of GSRMs, and  
 866 dots represent observed values. The shaded areas reflect the standard deviation among  
 867 the different GSRMs' simulations, indicating the spread of different models.  
 868  
 869  
 870



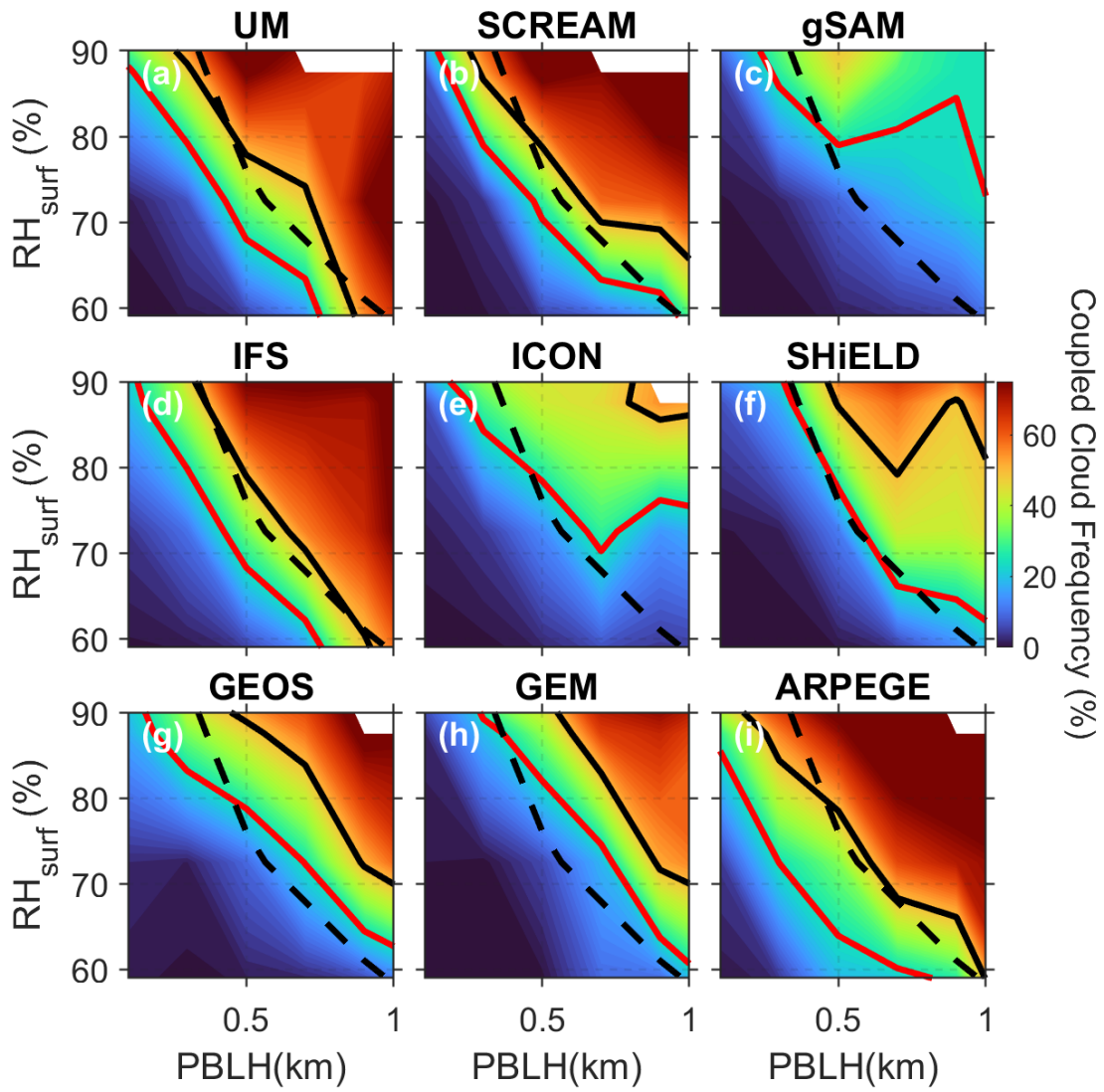
871

872 **Figure 11.** Diurnal variations in surface sensible heat (SH) and latent heat (LH) across  
 873 six geographical regions, as produced by various Global Storm-Resolving Models  
 874 (GSRMs) and compared to field observations (OBS). Each panel corresponds to  
 875 different sites: (a) SGP, (b) SAIL, (c) TRACER, (d) ENA, (e) GOAMAZON, and (f)  
 876 CACTI. Solid lines indicate the mean values of GSRMs, and dots represent observed  
 877 values. The shaded areas reflect the standard deviation among the different GSRMs'  
 878 simulations, indicating the spread of model outputs.  
 879



880

881 **Figure 12.** Contour plots illustrating the relationship between surface relative humidity  
 882 ( $\text{RH}_{\text{surf}}$ ) and planetary boundary layer height (PBLH) with the frequency of low clouds  
 883 for observed and modeled data. Panels (a) and (b) display the frequency for coupled  
 884 clouds, while panels (c) and (d) show the frequency for decoupled clouds. Observed  
 885 frequencies are represented in panel (a) and (c), and those simulated by Global Storm-  
 886 Resolving Models (GSRMs) are depicted in panel (b) and (d). The colored scale  
 887 indicates low cloud frequency, with cooler colors representing lower frequencies and  
 888 warmer colors higher frequencies. Various symbols denote the six field campaign sites:  
 889 SGP (triangle), SAIL (circle), TRACER (star), ENA (square), GOAMAZON (diamond),  
 890 and CACTI (pentagon). Black and red contour lines trace the areas where low cloud  
 891 frequencies reach 50% and 25%, respectively, serving as critical thresholds for  
 892 comparing observed and modeled coupled cloud.



893

894

**Figure 13.** Contour plots illustrating the relationship between surface relative humidity ( $\text{RH}_{\text{surf}}$ ) and planetary boundary layer height (PBLH) in determining the frequency of coupled clouds, as simulated by various Global Storm-Resolving Models (GSRMs). Each panel corresponds to a different GSRM: (a) UM, (b) SCREAM, (c) gSAM, (d) IFS, (e) ICON, (f) SHIELD, (g) GEOS, (h) GEM, and (i) ARPEGE. The color gradient indicates the cloud frequency percentage, with cooler colors representing lower frequencies and warmer colors indicating higher frequencies. Solid lines within each plot represent the 50% cloud frequency contour as derived from each respective model, while the dashed lines depict the 50% cloud frequency contour from observational data.